JACS
JOURNAL OF THE AMERICAN CHEMICAL SOCIETY
Article
pubs.acs.org/JACS

$[Fe^{IV}{=}O(TBC)(CH_3CN)]^{2+}$: Comparative Reactivity of Iron(IV)-Oxo Species with Constrained Equatorial Cyclam Ligation

Samuel A. Wilson,[†] Junying Chen,[‡] Seungwoo Hong,[‡] Yong-Min Lee,[‡] Martin Clémancey,[§] Ricardo Garcia-Serres,[§] Takashi Nomura,[∥] Takashi Ogura,[∥] Jean-Marc Latour,*[,§] Britt Hedman,*[,⊥] Keith O. Hodgson,*[,†,⊥] Wonwoo Nam,*[,‡] and Edward I. Solomon*[,†,⊥]

[†]Department of Chemistry, Stanford University, Stanford, California 94305, United States

[‡]Department of Bioinspired Science, Department of Chemistry and Nano Science, Center for Biomimetic Systems, Ewha Womans University, Seoul 120-750, Korea

[§]Laboratoire de Chimie de Biologie des Métaux, UMR 5249, Université Joseph Fourier, Grenoble-1, CNRS-CEA 17 Rue des Martyrs, 38054 Grenoble Cedex 9, France

[∥]Picobiology Institute, Graduate School of Life Science, University of Hyogo, Koto 3-2-1, Kamigori-cho, Ako-gun, Hyogo 678-1297, Japan

[⊥]Stanford Synchrotron Radiation Lightsource, SLAC National Accelerator Laboratory, Stanford University, Menlo Park, California 94025-7015, United States

Supporting Information

ABSTRACT: $[Fe^{IV}{=}O(TBC)(CH_3CN)]^{2+}$ (TBC = 1,4,8,11-tetrabenzyl-1,4,8,11-tetraazacyclotetradecane) is characterized, and its reactivity differences relative to $[Fe^{IV}{=}O(TMC)(CH_3CN)]^{2+}$ (TMC = 1,4,8,11-tetramethyl-1,4,8,11-tetraazacyclotetradecane) are evaluated in hydrogen atom (H-atom) abstraction and oxo-transfer reactions. Structural differences are defined using X-ray absorption spectroscopy and correlated to reactivities using density functional theory. The $S = 1$ ground states are highly similar and result in large activation barriers (~25 kcal/mol) due to steric interactions between the cyclam chelate and the substrate (e.g., ethylbenzene) associated with the equatorial π-attack required by this spin state. Conversely, H-atom abstraction reactivity on an $S = 2$ surface allows for a σ-attack with an axial substrate approach. This results in decreased steric interactions with the cyclam and a lower barrier (~9 kcal/mol). For $[Fe^{IV}{=}O(TBC)(CH_3CN)]^{2+}$, the $S = 2$ excited state in the reactant is lower in energy and therefore more accessible at the transition state due to a weaker ligand field associated with the steric interactions of the benzyl substituents with the trans-axial ligand. This study is further extended to the oxo-transfer reaction, which is a two-electron process requiring both σ- and π-electron transfer and thus a nonlinear transition state. In oxo-transfer, the $S = 2$ has a lower barrier due to sequential vs concerted ($S = 1$) two electron transfer which gives a high-spin ferric intermediate at the transition state. The $[Fe^{IV}{=}O(TBC)(CH_3CN)]^{2+}$ complex is more distorted at the transition state, with the iron farther out of the equatorial plane due to the steric interaction of the benzyl groups with the trans-axial ligand. This allows for better orbital overlap with the substrate, a lower barrier, and an increased rate of oxo-transfer.

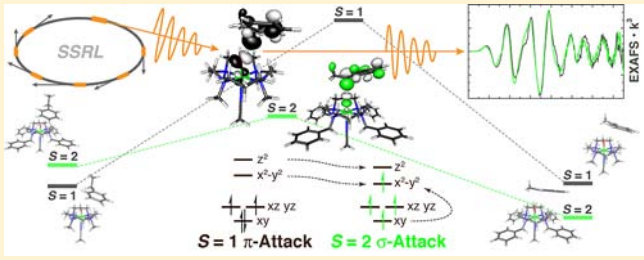

1. INTRODUCTION

High-valent iron−oxo groups have long been invoked as the active intermediates for many mononuclear nonheme iron enzymes,[1−3] catalyzing a wide variety of key biological reactions ranging from hydroxylation[4] to oxo-electrophilic aromatic attack.[5,6] Due to their important physiological functions, studies of these enzymes and their reactive intermediates have been an intense area of research focus. In recent years, Krebs, Bollinger, Hausinger, and their co-workers have successfully trapped and characterized iron(IV)−oxo intermediates in the active sites of α-ketogluterate-dependent and pterin-dependent enzymes including taurine: α-KG dioxygenase (TauD),[7−10] prolyl-4-hydroxylase (P4H),[11] halogenase CytC3,[5,6] tyrosine hydroxylase,[12] and recently phenylalanine hydroxylase.[13] However, due to the reactive nature associated with these intermediates, their detailed spectroscopic characterization has been challenging. Thus, biomimetic model studies of the nonheme $Fe^{IV}{=}O$ unit are an essential component for understanding geometric and electronic structure contributions to function.

To date, $Fe^{IV}{=}O$ model complexes have been structurally defined for both the low-spin (LS) $S = 1$[14−31] and high-spin (HS) $S = 2$[32−36] states. The majority of the models have an $S = 1$ ground state, while those defined for nonheme enzymes exhibit $S = 2$ ground states. It has been generally thought that

Received: May 17, 2012
Published: June 18, 2012

   dx.doi.org/10.1021/ja3046298 | J. Am. Chem. Soc. 2012, 134, 11791−11806

the high-spin $S = 2$ is more reactive than the low-spin $S = 1$ state. It has been proposed that this increased reactivity is due to an exchange stabilization of the high-spin d^4 configuration.[37] Alternatively, the role of the exchange stabilization can be to simply lower the energy of the α d_{z^2} σ^* orbital so that it is competitive with the β $d_{xz/yz}$ π^* frontier molecular orbitals (FMOs).[4,38] This would allow both σ- and π-type attack on the substrate, whereas for the $S = 1$, only the β π^* FMO is low in energy, and therefore only the π-attack is possible. It has been shown[39,40] that this π-attack requires a side-on approach of the substrate to achieve good orbital overlap with the oxo $p_{x/y}$ orbital. This can result in a large steric interaction between the substrate and an equatorial chelating ligand, raising the reaction barrier of the π-attack pathway. However, H-atom abstraction reactivity studies[34] on the $S = 2$ $[Fe^{IV}{=}O(TMG_3tren)]^{2+}$ (TMG_3tren =1,1,1-tris{2-[*N*2-(1,1,3,3-tetramethylguanidino)]ethyl}amine) complex find rates similar to those of $S = 1$ $[Fe^{IV}{=}O(N4Py)]^{2+}$ (N4Py = *N*,*N*-bis(2-pyridylmethyl)-*N*-bis(2-pyridyl)methyl-amine). This has been shown to be due to the significant steric bulk of the TMG_3tren ligand which limits substrate access even to the axial position of the enclosed Fe=O group.[34,37,40]

In the case of $[Fe^{IV}{=}O(TMC)(CH_3CN)]^{2+}$ (TMC = 1,4,8,11-tetramethyl-1,4,8,11-tetraazacyclotetradecane), which utilizes a 14-membered cyclam ring and has an $S = 1$ ground state,[18] the steric constraints of the cyclam equatorial ligand have been shown to greatly limit the approach and overlap of the substrate with the Fe=O unit required for π-attack.[39] As a result, $[Fe^{IV}{=}O(TMC)(CH_3CN)]^{2+}$ exhibits very low reactivity toward H-atom abstraction reactions and oxo-electrophilic attack (oxo-transfer). In the present study, $[Fe^{IV}{=}O(TBC)(CH_3CN)]^{2+}$ (TBC = 1,4,8,11-tetrabenzyl-1,4,8,11-tetraazacyclotetradecane), having an ever more bulky benzyl substituent on the cyclam framework, is observed to exhibit a substantial rate enhancement of more than 2 orders of magnitude over $[Fe^{IV}{=}O(TMC)(CH_3CN)]^{2+}$ for both H-atom and oxo-transfer reactions. X-ray absorption spectroscopy (XAS) measurements combined with density functional theory (DFT) calculations show that the bulky substituents on the TBC ligand weaken both the axial and equatorial ligand fields making the $S = 2$ state more accessible. This allows participation of the σ FMO for an axial substrate attack along the Fe=O bond and a lower steric contribution to the barrier at the transition state for the TBC complex. This model is then extended to oxo-electrophilic attack, formally a two-electron process, that requires both Fe=O π and σ orbital overlap with the substrate to facilitate reactivity. Again large differences are found for the $S = 1$ vs the $S = 2$ transition state barriers and for the TBC chelate relative to TMC. For oxo-transfer, these differences in barrier height are related to a concerted vs sequential electron-transfer associated with the different spin states and the different structural distortions at the transition state.

2. MATERIALS AND METHODS

Solvents were dried according to published procedures and distilled under argon prior to use.[41] All chemicals were obtained from Sigma-Aldrich Co. as the highest purity available and were therefore used without further purification unless otherwise indicated.

2.1. Synthesis of Materials. Nonheme ferrous complexes, $[Fe^{II}(TBC)(CH_3CN)](OTf)_2$ (**1**) (OTf = $CF_3SO_3^-$), $[Fe^{II}(TMC)(CH_3CN)](OTf)_2$, and $[Fe^{II}(N4Py)(CH_3CN)](OTf)_2$, and their respective oxo−iron complexes, $[Fe^{IV}{=}O(TBC)(CH_3CN)]^{2+}$ (**2**), $[Fe^{IV}{=}O(TMC)(CH_3CN)]^{2+}$, and $[Fe^{IV}{=}O(N4Py)]^{2+}$, were prepared according to literature methods.[16,18,42,43] Preparation and handling of all air-sensitive materials, such as $[Fe^{II}(TBC)(CH_3CN)](CF_3SO_3)_2$ and $[Fe^{II}(TMC)(CH_3CN)](CF_3SO_3)_2$, were done under an inert nitrogen atmosphere using a glovebox. The TBC ligand was synthesized by the reaction of cyclam (1.0 g, 5.0 mmol) and benzyl bromide (3.76 g, 22.0 mmol) in the presence of potassium carbonate (3.0 g, 22.0 mmol) in anhydrous *N*,*N*-dimethylformamide (DMF; 200 mL). The mixture was refluxed overnight under an argon atmosphere and then cooled to obtain a white precipitate at 60% of theoretical yield. The precipitate was then filtered and recrystallized from dichloromethane (CH_2Cl_2). **1** was prepared by the reaction between $Fe^{II}(OTf)_2$ (0.095 g, 0.268 mmol) and the TBC ligand (0.100 g, 0.178 mmol) in 2 mL acetonitrile (CH_3CN) in a glovebox at 25 °C. Single crystals of **1** were block shaped and colorless and were obtained by slow diffusion of diethyl ether (Et_2O) into concentrated CH_3CN solution of **1** under argon atmosphere at −30 °C. Intermediate **2** was generated by the addition of 2 equivalents of solid iodosylbenzene (PhIO)[44] into a solution of **1** in CH_3CN and was stirred for 10−20 min at 0 °C. PhIO was prepared according to literature method.[44]

2.2. Instrumentation. UV−vis spectra were recorded on a Hewlett-Packard 8453 diode array spectrophotometer equipped with a circulating water bath or UNISOKU cryostat system (USP-203; UNISOKU, Japan). Electrospray ionization mass (ESI-MS) spectra were collected on a Thermo Finnigan (San Jose, CA, USA) LCQ Advantage MAX quadrupole ion trap instrument, by manually infusing samples directly into the source. The spray voltage was set at 3.7 kV and the capillary temperature at 180 °C. Continuous wave electron paramagnetic resonance (CW-EPR) spectra were recorded at 5 K using an X-band Bruker EMX-plus spectrometer equipped with a dual mode cavity (ER 4116DM). Low temperatures were achieved and controlled with an Oxford Instruments ESR900 liquid He quartz cryostat with an Oxford Instruments ITC503 temperature and gas flow controller. The experimental parameters for the EPR spectra were as follows: Microwave frequency = 9.646 GHz, microwave power = 1 mW, modulation frequency = 100 kHz, and modulation amplitude = 10 G. Resonance Raman (rR) spectra were obtained using a liquid nitrogen cooled CCD detector (CCD-1024 × 256-OPEN-1LS, HORIBA Jobin Yvon) attached to a 1 m single polychromator (MC-100DG, Ritsu Oyo Kogaku) with a 1200 grooves/mm holographic grating. An excitation wavelength of 442 nm was provided by a Kr^+ laser (Spectra Physics, BeamLok 2060-RM), with 20 mW power at the sample point. All measurements were carried out with a spinning cell (1000 rpm) at −20 °C. Raman shifts were calibrated with indene, and the accuracy of the peak positions of the Raman bands was ± 1 cm^{-1}. Mössbauer spectra were measured either on a low-field Mössbauer spectrometer equipped with a Janis SVT-400 cryostat or an Oxford Instruments Spectromag 4000 cryostat containing an 8 T split-pair superconducting magnet. Both spectrometers were operated in constant acceleration mode in transmission geometry. The isomer shifts are referenced against a room-temperature metallic iron foil. Analysis of the data was performed using the program WMOSS (WEB Research).

2.3. Spin State Measurements. ^{1}H NMR spectra were measured using a Bruker AVANCE III 400 MHz spectrometer. The effective magnetic moments (μ_{eff}, BM) of complexes **1** and **2** were determined using the modified method of Evans at room temperature and 15 °C, respectively.[45−47] A WILMAD coaxial insert (sealed capillary) tube containing the blank acetonitrile-d_3 solvent (with 1.0% tetramethylsilane (TMS)) only was inserted into the normal NMR tubes containing the complexes (4 mM) dissolved in acetonitrile-d_3 (with 0.05% TMS). The chemical shift of the TMS peak (and/or solvent peak) in the presence of the paramagnetic metal complexes was compared to that of the TMS peak (and/or solvent peak) in the inner coaxial insert tube.

2.4. X-ray Structural Analysis. Single crystals of **1** suitable for X-ray analysis were obtained by slow diffusion of Et_2O into an CH_3CN solution of **1**. A single crystal was then mounted on a glass fiber tip with epoxy cement. Diffraction data were collected at 100 K on a Bruker SMART AXS diffractometer equipped with a monochromator in the Mo Kα (λ = 0.71073 Å) incident beam. The CCD data were

integrated and scaled using the Bruker-SAINT software package, and the structure was solved and refined using SHEXTL V 6.12.[48] H-atoms were located in the calculated positions. Crystal data for **1**·$(CH_3CN)_2$: $C_{46}H_{57}F_6FeN_7O_6S_2$, triclinic, P_{-1}, Z = 2, a = 12.1461(18), b = 13.876(2), c = 17.131(3) Å, α = 67.041(8), β = 72.676(9), γ = 67.039(8)°, V = 2411.7(6) Å^3, μ = 0.478 mm^{-1}, d_{calc} = 1.429 g/cm^3, R_1 = 0.0733, wR_2 = 0.1734 for 6152 unique reflections, 616 variables. The CCDC (875224) contains the supplementary crystallographic data for **1**. These data can be obtained free of charge via www.ccdc.cam.ac.uk/data_request/cif or from the Cambridge Crystallographic Data Centre, 12, Union Road, Cambridge CB2 1EZ, UK; fax: (+44) 1223-336-033; e-mail: deposit@ccdc.cam.ac.uk.

2.5. Reactivity Studies. All reactions were followed using a Hewlett-Packard 8453 spectrophotometer to monitor UV−vis spectral changes of the reaction solutions. $[Fe^{IV}{=}O(L)]^{2+}$ (L = TBC, TMC, and N4Py) species were generated in the reaction of $[Fe^{II}(L)(CH_3CN)](OTf)_2$ with 2 equivalents of solid PhIO in CH_3CN at 0 or 15 °C. The solutions were then filtered for further utilization. Kinetic measurements for C−H activation of ethylbenzene and sulfoxidation of thioanisole by $[Fe^{IV}{=}O(L)]^{2+}$ were carried out in CH_3CN at 15 °C under pseudo-first-order conditions, where the concentrations of substrates were maintained in greater than 10-fold excess relative to the $[Fe^{IV}{=}O(L)]^{2+}$ (5.0×10^{-4} or 1.0×10^{-3} M, respectively). Rates were monitored by the decay of absorption bands at 885 nm due to $[Fe^{IV}{=}O(TBC)]^{2+}$, 820 nm due to $[Fe^{IV}{=}O(TMC)]^{2+}$, and 695 nm due to $[Fe^{IV}{=}O(N4Py)]^{2+}$, respectively. All reactions were run at least in triplicate, and the data reported here represent the average of these reactions.

2.6. XAS Measurements. Samples were prepared and frozen under liquid nitrogen in several 2 × 10 mm pinhole-type Delrin cells wrapped with Kapton tape. Samples were oriented at 45° to the incident X-ray beam and maintained at 10 K using an Oxford Instruments CF1208 continuous flow liquid helium cryostat. XAS data were collected at beamline 9-3[49] at the Stanford Synchrotron Radiation Lightsource (SSRL) under ring operating conditions of 150−200 mA over an energy range of 6785−8000 eV (k = 15 Å^{-1}) for all complexes. Fluorescence data were collected at 90° to the incident beam using a solid-state 30-element Ge detector array with Soller slits and a 6 wavelength Mn filter aligned between the detector and the sample to improve the Fe Kα fluorescence signal intensity relative to that of the scattered beam.[50] For all data sets an internal calibration was utilized with the first inflection point of an Fe foil set to 7111.20 eV.[51]

During measurements, the data in the Fe K-edge, K pre-edge, and extended X-ray absorption fine structure (EXAFS) regions were continuously monitored in order to ensure sample integrity by comparing each individual scan to ones taken previously. No sample degradation was observed for the ferrous starting complex $[Fe^{II}(TBC)(CH_3CN)]^{2+}$ (**1**), and all scans were included in the final average (15 scans). For $[Fe^{IV}{=}O(TBC)(CH_3CN)]^{2+}$ (**2**) significant photoreduction was observed, and data collection was limited to 2 scans per spot with 4 separate 1 × 4 mm spots per each 2 × 10 mm XAS cell (12 scans total). While no photoreduction or change in the EXAFS signal was evident for **2**, a negative shift of ∼0.4 eV per-scan was observed in the K-edge energy. As a result, the K-edge data presented in this study are the average of only the first scan on each spot. Iron K-edge, pre-edge, and EXAFS data were also measured for $[Fe^{IV}{=}O(TMC)(CH_3CN)]^{2+}$ to allow for a direct comparison to this closely related $Fe^{IV}{=}O$ system.

2.7. XAS Data Processing. Data reduction, background subtraction, and normalization were performed according to established methods[52−54] using the program PySpline,[55] with the data normalized to a value of 1.0 at 7130.0 eV. The spline function through the EXAFS region was chosen to minimize any residual low-frequency background but not reduce the EXAFS amplitude, as monitored by the Fourier transform intensity. For pre-edge and edge analysis, all data sets were truncated to k = 9.5 Å^{-1} and renormalized using a third-order post-edge polynomial background and a two-segment (three knot) spline for comparison between data sets and to past reference compounds.[56] Normalization of the EXAFS data was accomplished using a second-order post-edge polynomial background fit over the full data range (k = 15 Å^{-1}) and a three-segment (four knot) spline. Normalization was also tested using a four-segment (five knot) spline, however, this resulted in no appreciable change in either the EXAFS or its associated Fourier transform, and therefore the three-segment spline was used in the final analysis.

Iron K pre-edge features were modeled with a pseudo-Voigt line shape in a 50:50 ratio of Lorentzian:Gaussian functions using the fitting program EDG_FIT[57] as part of the program suite EXAFSPAK.[58] The energy position, full width at half-maximum (fwhm), and peak intensity were all allowed to float throughout the fitting process. A function modeling the background was empirically chosen to give the best fit, floated with all variables, and then varied with different fwhm (± 0.5 fixed from float) to establish confidence limits on pre-edge intensity. In all cases, an acceptable fit reasonably matched both the pre-edge data as well as those of its second derivative. A minimum of three fits with different fwhm (± 0.5 fixed from float) backgrounds were acquired over the energy ranges of 7108−7116, 7108−7117, and 7108−7118 eV for **1** and 7108−7117, 7108−7118, and 7108−7119 eV for **2** to provide at least 9 pre-edge fits per data set. These were then averaged to give the final pre-edge energy and intensity values.

EXAFS signals were calculated using FEFF (version 7.0), and the data were fit using the program OPT as part of EXAFSPAK.[58] In all fits the bond lengths (R) and bond variances (σ^2) were allowed to vary, with the initial value for bond variance set to 0.005 Å^2, even for fits where single and multiple scattering (SS and MS, respectively) paths were related to one another. The threshold energy (k = 0, E_0) was also allowed to vary but was constrained as a common variable (ΔE_0) for all fit paths in a given data set. The amplitude reduction factors (S_0^2) were fixed to a value of 1.0, and the coordination numbers (CN) were varied systematically based on a structural model to achieve the best fit to the EXAFS data. The best choice of all available FEFF paths and the goodness of the overall fit were optimized based on a combination of weighted F-factor (F) as well as visual fit to the EXAFS data and their Fourier transform. On the basis of studies of complexes of known structures, the uncertainties in final distances are within 0.02 Å.

The EXAFS data for **1** were fit using both the crystallographic structure as well as a DFT geometry optimized structure (vide infra) as initial models for $[Fe^{II}(TBC)(CH_3CN)]^{2+}$. In either case, the similarity between the optimized geometry and the crystal structure gave the same values for the final EXAFS fit. In the case of intermediate **2**, where a crystal structure is not currently available, the EXAFS data were fit to the computational model (vide infra).

2.8. DFT Calculations. All complexes used in EXAFS modeling and reactivity studies were fully optimized using Gaussian 03[59] and the unrestricted hybrid density functional UB3LYP[60] (three-parameter Becke GGA exchange modified to include Hartree−Fock mixing with Lee, Yang, and Parr correlation)[61,62] with the 6-311G(d) basis set. Single point energies on final geometries were calculated using an expanded basis set of 6-311+G(2df,2pd) with solvent corrections (PCM = acetonitrile) and frequencies calculated with 6-311G(d). In some cases, calculations were also done using UBP86/6-311G(d) (Becke GGA exchange[63] with Perdew 1986 nonlocal correlation)[64] as a comparison between functionals. However, BP86 tended to overstabilize the low-spin ground state resulting in a large energy splitting between spin states, and in some cases this lead to an incorrect ground state. In addition, B3LYP gave optimized geometries that were more consistent with the EXAFS data, and thus, B3LYP was utilized for the reaction coordinate and transition state calculations. It should be noted that the energetic trend between the S = 1 and 2 states for both $[Fe^{IV}{=}O(TBC)(CH_3CN)]^{2+}$ and $[Fe^{IV}{=}O(TMC)(CH_3CN)]^{2+}$ was consistent regardless of functional.

Transition state geometries were calculated by positioning a preoptimized substrate molecule above the $[Fe^{IV}{=}O(L)]^{2+}$ intermediate at an appropriate distance with the benzylic hydrogen of ethylbenzene or the sulfur of thioanisole oriented toward the Fe=O group along the desired reaction coordinate. In the case of ethylbenzene, the Fe=O and the C−H bonds were lengthened and

frozen in place while allowing the rest of the system to optimize. Once this starting structure converged, frequencies were checked, and if reasonable, a search for the transition state was performed without constraints using the B3LYP/6-311G(d) level of theory. All transition state structures had only one imaginary frequency (along the desired reaction coordinate). Reactant and product complexes were then calculated by following the intrinsic reaction coordinate (IRC) in the forward and reverse directions and then optimizing to the final complexes that contained all real frequencies. Again, final energies were obtained using a larger basis set, 6-311+G(2df,2pd), with corrections for zero point energy, entropy, and solvent (PCM = acetonitrile) performed using the 6-311G(d) basis set. Calculations were analyzed using QMForge[65] and plotted using a combination of gOpenMol[66,67] and MacPyMol.[68]

3. RESULTS AND ANALYSES

3.1. Characterization of $[Fe^{II}(TBC)(CH_3CN)]^{2+}$.

$[Fe^{II}(TBC)(CH_3CN)](OTf)_2$, (**1**), was synthesized by reacting equimolar amounts of $Fe^{II}(OTf)_2$ and the TBC ligand in CH_3CN at 25 °C and was characterized by EPR, NMR, ESI-MS, Mössbauer, XAS, and X-ray crystallography.

The ESI-MS spectrum of **1** exhibits three prominent ion peaks at *m*/*z* 308.2, 328.6, and 765.3, Supporting Information (SI) Figure 1, whose mass and isotope distribution patterns correspond to $[Fe^{II}(TBC)]^{2+}$ (calcd *m*/*z* 308.2), $[Fe^{II}(TBC)(CH_3CN)]^{2+}$ (calcd *m*/*z* 328.7), and $[Fe^{II}(TBC)(OTf)]^{+}$ (calcd *m*/*z* 765.3). The X-band EPR spectrum of **1** exhibited no signals, SI Figure 2, which is consistent with **1** being an integer spin ferrous system. The spin state of **1** (in CH_3CN) was determined using the ^{1}H NMR Evans method[45−47] and gave a room-temperature magnetic moment of 5.4 μ_B, which indicates a high-spin (*S* = 2) ferrous species.

The high-spin state of **1** was additionally confirmed by Mössbauer spectroscopy (SI Figure 3). The 4.2 K spectrum shows several quadrupole doublets that were fit with two asymmetric quadrupole doublets whose large isomer shifts and quadrupole splittings (SI Table 1) can only be assigned to high-spin ferrous centers. The presence of two different doublets may be attributed to the existence of different configurational isomers in solution, **1a** and **1b**. The spectrum of **1b** shows an unusually large quadrupole splitting, which could result from a constrained geometry, resulting in a very anisotropic EFG. An additional proof of the *S* = 2 ground state of **1** was obtained by measuring Mössbauer spectra in strong applied magnetic fields (SI Figure 4). These data were incompatible with anything other than a spin quintet.

Single crystals of **1** suitable for crystallographic analysis were obtained by the diffusion of Et_2O into an CH_3CN solution of **1**. The X-ray crystal structure shows a ferrous center penta-coordinated by the four nitrogen atoms of the TBC ligand and one axial acetonitrile from the solvent orientated *syn* relative to the benzyl groups of the cyclam. The coordination geometry around the iron is best described as being between a trigonal-bipyramidal and a square-based pyramidal structure, with a τ value of 0.52 (Figure 1).

Comparison of the XAS data for **1** to high-spin $[Fe^{II}(TMC)(CH_3CN)]^{2+}$ shows that the K pre-edge and edge spectra nearly superimposed,[56] with slightly more intensity for **1** (Figure 2). By comparison, $[Fe^{II}(tacn)_2]^{2+}$ (tacn = 1,4,7-triazacyclononane) and $[Fe^{II}(BQEN)(CH_3CN)_2]^{2+}$ (BQEN = *N*,*N*′-dimethyl-*N*,*N*′-bis(8-quinolyl)ethane-1,2-diamine), two low-spin ferrous compounds,[14,56] exhibit K-edge features which are shifted to higher energy relative to **1** and with diminished pre-edge intensities reflecting the fact that these low-spin ferrous complexes are six coordinate and are therefore more centrosymmetric. The pre-edge of **1** exhibits two features centered at 7111.7 and 7113.8 eV with intensities of 12.0 and 4.5 units, respectively, for a total intensity of 16.5 (1.8) normalized units (Table 1 and SI Figure 5). This is greater than the total intensity of 12.7 (0.5) units for $[Fe^{II}(TMC)(CH_3CN)]^{2+}$, indicating that relative to $[Fe^{II}(TMC)(CH_3CN)]^{2+}$, **1** has a larger amount of 3d/4p mixing and thus a higher degree of structural distortion.[56]

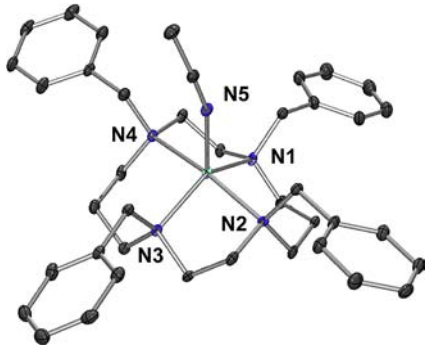

Figure 1. ORTEP-3 diagram of **1**, $[Fe^{II}(TBC)(CH_3CN)]^{2+}$ with 30% probability displacement ellipsoids. H-atoms have been omitted for clarity. Selected bond distances (Å): Fe−N1 2.143(4), Fe−N2 2.258(3), Fe−N3 2.141(4), Fe−N4 2.290 (3), and Fe−N5 2.063(4).

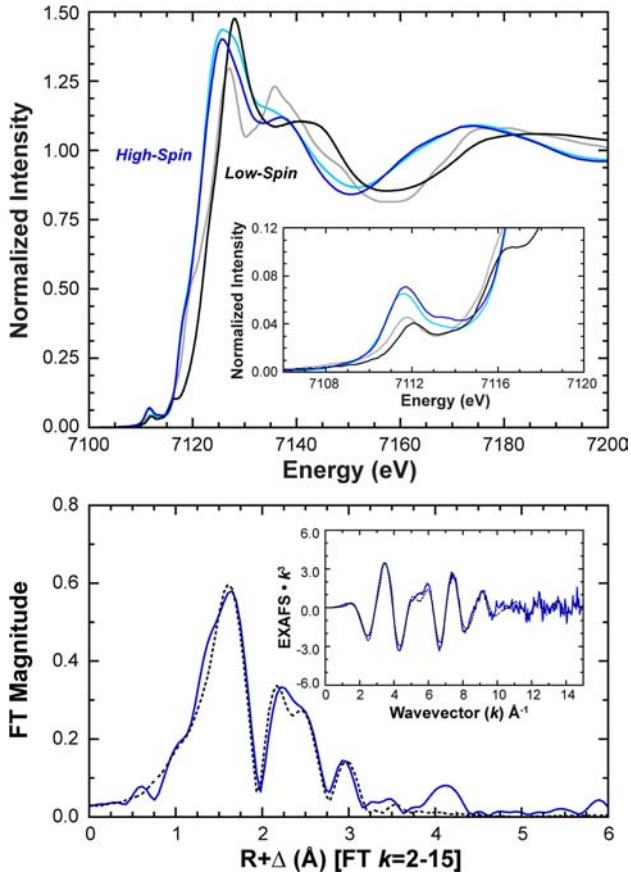

Figure 2. Top: Fe K-edge (top) and pre-edge (inset) XAS spectra of **1** (blue) compared with high-spin $[Fe^{II}(TMC)(CH_3CN)]^{2+}$ (light-blue) and low-spin $[Fe^{II}(BQEN)(CH_3CN)_2]^{2+}$ (black) and $[Fe^{II}(tacn)_2]^{2+}$ (gray) reference compounds. Bottom: Fourier transform and EXAFS (inset) data (—) and fit (----) of **1**.

Table 1. XAS Pre-Edge Energy and Intensity[a]

	peak 1 (eV)	area	peak 2 (eV)	area	total intensity
1	7111.7	12.0	7113.8	4.5	16.5 ± 1.8
2	7113.0	25.1	7114.0	8.6	33.7 ± 2.5

[a]Fe K pre-edge fits for **1** and **2**. Peak energies are listed at maximum, areas are multiplied by 100 for convenience and comparison to previously published data. Total intensity is the sum of both areas. Error values are calculated from total intensity standard deviations across all nine fits. Pre-edge fits are shown in SI Figure 5.

EXAFS data for **1** were collected to k = 15 Å^{-1} and exhibit a well-defined beat pattern out to ~k = 10 Å^{-1}, giving rise to two main features in the Fourier transform (FT) (Figure 2). The first shell EXAFS data were best fit using a five coordinate (5C) 1:4 split shell at an average distance of 2.20 Å (CN = 4) with a single shorter path at 2.07 Å. These EXAFS distances are in excellent agreement with the crystallographic data (vide supra) that show four Fe−N TBC distances at an average of 2.22 Å and a short Fe−CH_3CN at 2.06 Å. These distances are also consistent with those of other high-spin ferrous systems, including other TMC complexes.[24,69] The second shell EXAFS features were fit by the addition of eight SS carbon-based pathways from TBC at a distance of 3.01 Å, followed by a complementary set of 24 MS paths at 3.33 Å with a corresponding bond variance of 375 (fit 1-1, Table 2 and Figure 2). Alternatively, the outer sphere MS contribution could be fit using only two high-intensity forward focused MS paths from the axial CH_3CN at a distance of 3.41 Å with a bond variance of 393 (fit 1-2, Table 2). However, the fits could not simultaneously support both types of MS paths given the similar distance and limited k-range of the data. Yet from the low bond variances that result when only one path is chosen, it is likely that the outer sphere EXAFS signals are in fact combinations of both TBC and CH_3CN MS contributions. Taken together, these XAS data independently define **1** as a distorted five-coordinate high-spin ferrous complex; a structural description for **1** in solution (acetonitrile) that is consistent with its solid-phase X-ray structure (Figure 1).

3.2. Characterization of $[Fe^{IV}{=}O(TBC)(CH_3CN)]^{2+}$.

Intermediate **2** was generated by an oxo-transfer reaction between **1** and PhIO and was characterized using a variety of spectroscopic techniques. The reaction of **1** with 2 equivalents of PhIO in CH_3CN at 15 °C produced a green intermediate, **2**, with λ_{max} at 885 nm (ε = 360 M^{-1} cm^{-1}; Figure 3A) and a relatively stable half-life of $t_{1/2}$ ≈ 40 min at 15 °C.

Intermediate **2** showed a radically different UV−vis spectrum from **1** (Figure 3A), with an intense feature at 885 nm that decayed over time. The ESI-MS spectrum of **2** exhibits one prominent isotope sensitive ion peak centered at m/z 781.2, whose mass and distribution patterns correspond to $[Fe^{IV}{=}O(TBC)(OTf)]^+$ (calcd m/z 781.3) (Figure 3B). Upon introduction of ^{18}O into **2**, the ion peak shifts up to m/z 783.2, indicating that **2** contains an iron−oxo group. The rR spectrum of **2**, measured in CH_3CN at −20 °C with 442 nm laser excitation, exhibits a doublet of peaks at 837 and 847 cm^{-1} arising from a Fermi resonance with an average peak position at 842 cm^{-1} that shifts to a single peak at 804 cm^{-1} upon introduction of ^{18}O (Figure 3C). The observed isotopic shift of −38 cm^{-1} with ^{18}O substitution is in good agreement with the calculated value ($\Delta\nu_{calcd}$ = −37 cm^{-1}) for the Fe=O diatomic harmonic oscillator.

Table 2. Final EXAFS Fits for 1 and 2[a]

$[Fe^{II}(TBC)(CH_3CN)]^{2+}$ (**1**)							
fit 1-1	CN	R (Å)	σ^2 (Å^2)	fit 1-2	CN	R (Å)	σ^2 (Å^2)
Fe−N	1	2.07	317	Fe−N	1	2.06	302
Fe−N	4	2.20	642	Fe−N	4	2.19	628
Fe−TBC	8	3.01	803	Fe−TBC	8	3.00	1242
TBC MS	24	3.33	375	CH_3CN MS	2	3.41	393
E_0 = −6.0		Error = 0.264		E_0 = −6.0		Error = 0.301	
$[Fe^{IV}{=}O(TBC)(CH_3CN)]^{2+}$ (**2**)							
fit 2-1	CN	R (Å)	σ^2 (Å^2)	fit 2-2	CN	R (Å)	σ^2 (Å^2)
Fe=O	1	1.64	339	Fe=O	1	1.64	339
Fe−N	5	2.10	556	Fe−N	5	2.11	559
Fe−TBC	8	2.94	1147	Fe−TBC	8	2.99	1030
TBC MS	24	3.16	373	CH_3CN MS	2	3.20	483
Fe−TBC	6	3.56	1370	Fe−TBC	6	3.48	1752
E_0 = −5.3		Error = 0.252		E_0 = −4.9		Error = 0.265	
$[Fe^{IV}{=}O(TMC)(CH_3CN)]^{2+}$							
fit 3-1	CN	R (Å)	σ^2 (Å^2)	fit 3-2	CN	R (Å)	σ^2 (Å^2)
Fe=O	1	1.63	445	Fe=O	1	1.63	441
Fe−N	5	2.09	522	Fe−N	5	2.09	524
Fe−TMC	8	2.95	935	Fe−TMC	8	3.00	1111
TMC MS	24	3.18	362	CH_3CN MS	2	3.22	304
Fe−TMC	6	3.55	1360	Fe−TMC	6	3.48	1021
E_0 = −4.2		Error = 0.249		E_0 = −3.8		Error = 0.254	

[a]All distances are in Å. σ^2 values are multiplied by 10^5 for convenience. All paths are considered SS paths unless otherwise indicated as MS. CN = coordination number. Error (F) is defined as $F = [\sum k^6(\chi_{exp} - \chi_{obs})^2/\sum k^6(\chi_{exp})]^{1/2}$.

dx.doi.org/10.1021/ja3046298 | J. Am. Chem. Soc. 2012, 134, 11791−11806

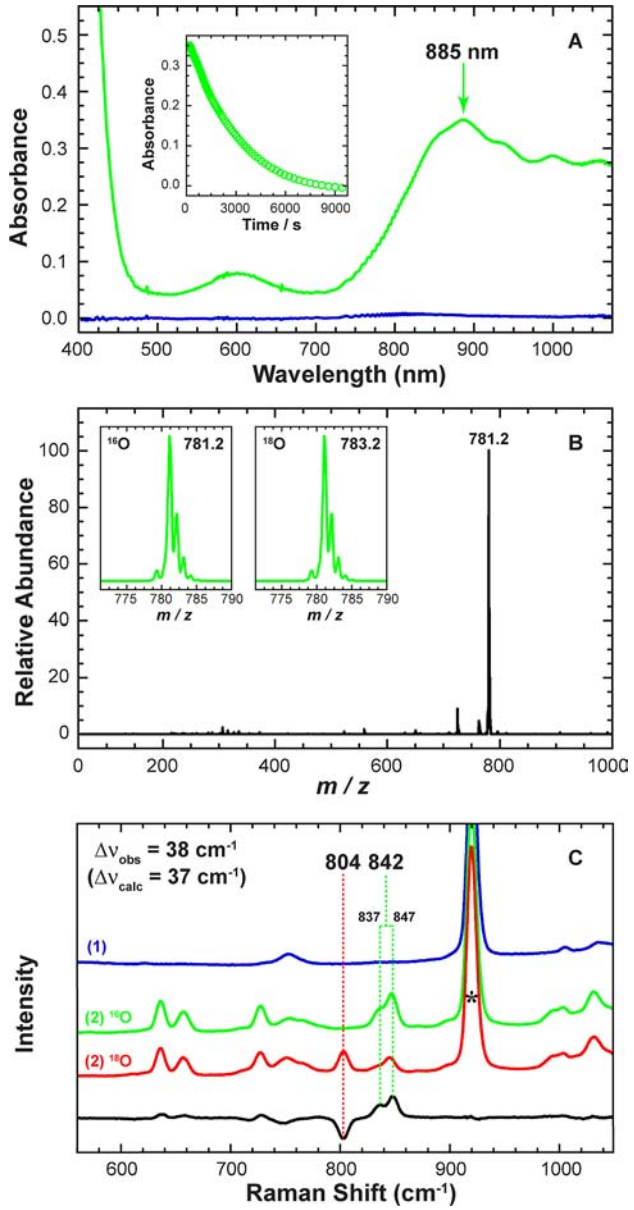

Figure 3. (A) UV−vis spectra of **1** (blue) vs intermediate **2** (green). **2** was generated in the reaction of **1** (1.0 mM) and 2 equivalents of PhIO in CH_3CN at 15 °C. The inset shows the natural decay of **2** monitored at 885 nm ($t_{1/2} \approx 40$ min). (B) EIS-MS spectrum of intermediate **2**. Inset shows observed isotope distribution patterns of **2** in ^{16}O (left) and ^{18}O (right). **2**-^{18}O was generated in the reaction of **1** (0.50 mM) and 2 equivalents of PhIO in the presence of $H_2{}^{18}O$ in CH_3CN at 15 °C. (C) Resonance Raman spectra of **1** (blue) and **2** prepared in the presence of $H_2{}^{16}O$ (green) and $H_2{}^{18}O$ (red) showing the isotope sensitivity of the 842 cm^{-1} band. The black line shows the intensity difference between **2**-^{16}O and **2**-^{18}O. The peak marked with * is from solvent.

The X-band EPR spectrum of **2** is silent (SI Figure 2), consistent with **2** being an integer spin system. The spin state of **2** (in CH_3CN) was determined using the ^1H NMR Evans method[45−47] and gave a magnetic moment of 3.3 μ_B at 15 °C, which indicates that **2** is a low-spin ($S = 1$) Fe^{IV}=O species.

The Mössbauer spectrum of **2** (SI Figure 3) is dominated by a quadrupole doublet that can be assigned to an Fe^{IV}=O based on its Mössbauer parameters (Table 3 and SI Table 1). Additionally, a smaller feature at high energy can be discerned,

Table 3. Mössbauer and Spin-Hamiltonian Parameters for TMC and TBC Fe^{IV}=O ($S = 1$) Complexes[a]

	$[Fe^{IV}$=O(TBC)$]^{2+}$ (**2**)	$[Fe^{IV}$=O(TMC)$]^{2+}$
D (cm^{-1})	29.5 ± 1.5	28
E/D	0[b]	0[b]
g_x, g_y, g_z	2.3, 2.3, 2.0[c]	2.3, 2.3, 2.0[c]
$A_{x,y,z}/g_N\beta_N$ (T)	−18 ± 1, −18[d], −2 ± 5	−25, −20, −5
δ (mm/s)	0.22 ± 0.01	0.17
ΔE_Q (mm/s)	0.97 ± 0.01	1.24
η	0.36 ± 0.3	0.50

[a]Mössbauer and spin-Hamiltonian parameters for **2** vs $[Fe^{IV}$=O(TMC)$(CH_3CN)]^{2+}$ (from literature).[17,18] Data collected on frozen CH_3CN solution at 4.2 K. [b]Fixed. [c]Calculated from ligand field treatment.[71] [d]$A_x = A_y$ fixed. Data and fit are shown in SI Figure 3 and Figure 4 in text.

representing a minor contribution of a high-spin ferrous species, with parameters corresponding to those of **1** (SI Figures 3 and 6). To further characterize **2**, field-dependent experiments were performed at 4.2 K in magnetic fields of 60 mT, 4 T, and 7 T applied parallel to the γ-rays (Figure 4A−C). The experiment that yielded the highest proportion of oxoferryl intermediate (78%) also yields a 1:1 ratio of **1a**:**1b**, similar to

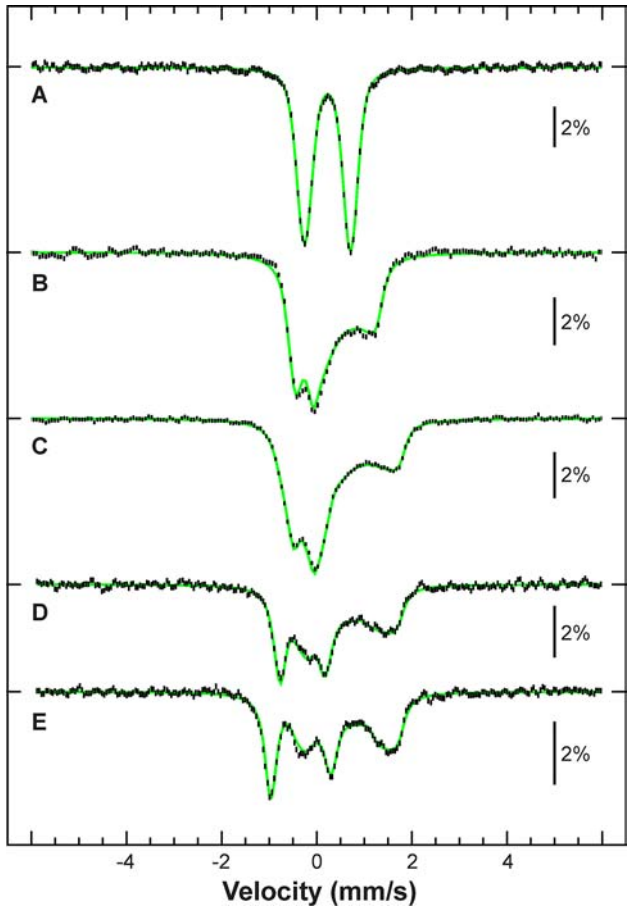

Figure 4. Mössbauer spectra of **2** (vertical bars), obtained by subtraction of a 22% contribution of **1** measured under identical conditions. Spectra measured at (A−C) 4.2 K, (D) 41 K, or (E) 78 K in a magnetic field of (A) 60 mT, (B) 4 T, or (C−E) 7 T applied parallel to the γ-rays. Spin-Hamiltonian simulation (green) was fit with a unique set of parameters for all spectra (Table 3), with (A) fit to an asymmetric quadrupole doublet.

dx.doi.org/10.1021/ja3046298 | J. Am. Chem. Soc. 2012, 134, 11791−11806

that found in the starting material. It should be noted that no ferrous contaminant was observed in the XAS data (vide infra). Therefore, a synthetic spectrum of **2** was constructed by subtracting a 22% contribution of **1** measured under identical conditions. The procedure is validated by the resultant flat baseline. The synthetic spectrum was fit with one unique set of spin-Hamiltonian parameters corresponding to an axially distorted $S = 1$ ground state (Figure 4).[70] Temperature-dependent spectra (Figure 4D,E) were also measured to assess the zero-field splitting and could be framed between 28 and 31 cm^{-1}. The spectra were therefore fit assuming $D = 29.5$ cm^{-1}, $E/D = 0$, $g_x = g_y = 2.3$, and $g_z = 2.0$[71] and afforded hyperfine parameters of $A_{x,y,z}/g_N\beta_N = (-18, -18, -2)$ T and $\eta = 0.36$. These results are also consistent with the NMR data and therefore **2** can be described as an $S = 1$ Fe^{IV}═O species.

To confirm the identity of **2**, Fe K pre-edge and edge XAS data were measured (Figure 5). Compared to **1**, the XAS data are shifted to higher energy, indicative of an increase in Z_{eff} for the iron, a change that is also consistent with the Mössbauer assignment of an Fe^{IV} oxidation state. Additionally, the pre-edge of **2** exhibits a large increase in intensity and was fit with two features having 25.1 and 8.6 intensity units, centered at 7113.0 and 7114.0 eV for a total intensity of 33.7 (2.5) units (Table 1 and SI Figure 5). This is more than double the pre-edge intensity of **1** (16.5 units) and is indicative of the formation of an Fe^{IV}═O species, as the presence of a short and highly covalent Fe═O bond increases the pre-edge intensity through additional 4p mixing into the 3d manifold.[56] A pre-edge intensity of 33.7 units is comparable to, but larger than, values observed for other six coordinate (6C) nonheme Fe^{IV}═O complexes;[17,18,72] in particular $[Fe^{IV}$═$O(TMC)(CH_3CN)]^{2+}$ (included as a reference in Figure 5), which has an established value of 30.0 units (SI Table 2),[17] indicating **2** contains a more distorted metal site and/or a more covalent Fe═O bond.

EXAFS data for **2** were measured up to $k = 15$ $Å^{-1}$ and are shown along with the final EXAFS fit in Figure 5 with fit parameters given in Table 2 and a comparison to **1** in SI Figure 7. Unlike the EXAFS of **1**, which greatly diminished around $k = 10$ $Å^{-1}$, the EXAFS of **2** have a strong and distinctive beat pattern all the way to $k = 15$ $Å^{-1}$ that gives rise to two main features in the Fourier transform. The first feature around ~1.5 Å ($R + \Delta$) has two prominent peaks which are a result of two closely spaced overlapping waves that are only individually resolved due to the high k-range of the data and large distance between two groups of absorber-scatter atom pairs. The second feature around ~2.7 Å ($R + \Delta$) is also resolvable into two features, both of which, similar to **1**, are likely to be from a combination of outer shell SS and MS contributions from the TBC cyclam ring.

Based on the above spectroscopic characterization of **1** and **2**, the EXAFS data were fit to a computational model (vide infra) of $[Fe^{IV}$═$O(TBC)(CH_3CN)]^{2+}$. EXAFS fits determined a 1:5 split first shell with a single short path at 1.64 Å and 5 Fe−N SS atoms at an average distance of 2.11 Å. In order to test this coordination number, a 1:4 fit was also tried. However, this coordination resulted in an unreasonably low bond variance for the four remaining nitrogen atoms, a worse error, and an EXAFS fit with inadequate beat pattern intensity. Considered along with the pre-edge intensity (33.7 units), which is considerably lower than that of a 5C Fe^{IV}═O complex,[28] these data exclude a 5C structure. The second shell EXAFS feature was fit in an analogous fashion to **1** using either an 8:24

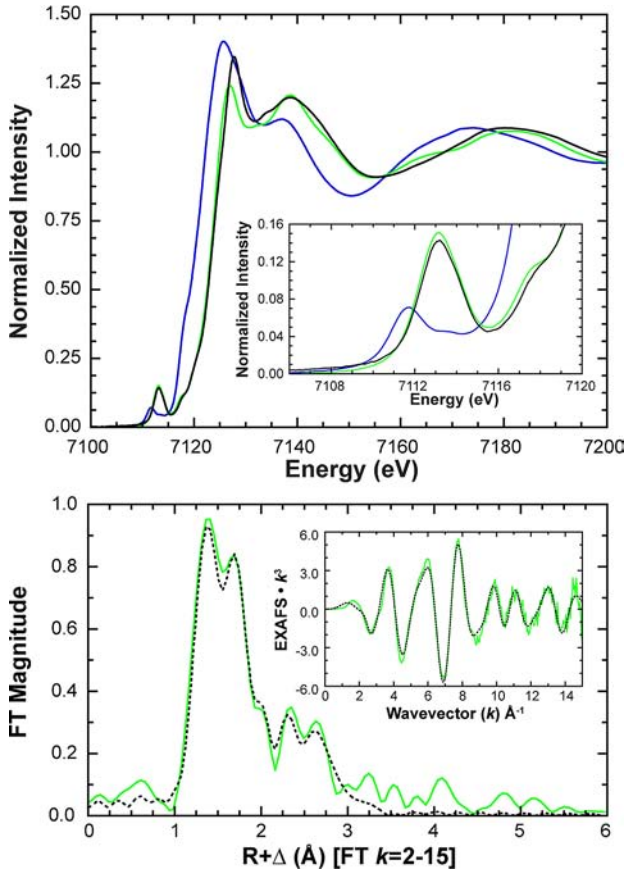

Figure 5. Top: Fe K-edge and enlarged pre-edge (inset) showing the increased pre-edge intensity of **2** (green) relative to **1** (blue) upon reaction with PhIO in acetonitrile. XAS data of $[Fe^{IV}$═$O(TMC)(CH_3CN)]^{2+}$ (black) are included for reference. Bottom: Fourier transform and EXAFS, data (—) and fit (----), of **2** showing the strong first-shell intensity contribution resulting from a short (1.64 Å) Fe═O bond.

SS:MS path ratio for TBC (fit 2-1 in Table 2) or only two MS paths from the axial CH_3CN (fit 2-2 in Table 2). Analogous to the final fit of **1**, using only two MS contributions from CH_3CN gave similar bond variances as 24 MS paths from TBC. However, the overall fit quality was worse, suggesting that while there are MS contributions from the axial CH_3CN ligand, the majority of the contribution originates from the cyclam ring. To arrive at a final structure, six more SS paths were added at a distance of 3.56 Å to account for both the benzyl carbons, and distal carbon atoms of the TBC ring. Similar to the pre-edge and edge energy and intensity, these EXAFS distances are consistent with those distances found for other 6C $S = 1$ Fe^{IV}═O complexes[17,18,22,72] including $[Fe^{IV}$═$O(TMC)(CH_3CN)]^{2+}$ for which a crystal structure is available. Combined, these data confirm that a new Fe^{IV}═O model complex has been successfully synthesized using the more sterically strained TBC ligand and identify intermediate **2** as $[Fe^{IV}$═$O(TBC)(CH_3CN)]^{2+}$ (Figure 6).

For a direct comparison between **2** and $[Fe^{IV}$═$O(TMC)(CH_3CN)]^{2+}$, analogous EXAFS data were also measured for $[Fe^{IV}$═$O(TMC)(CH_3CN)]^{2+}$ (SI Figure 8) and fit in an identical way as for **2** but using a geometry optimized model based on the known crystal structure.[18] EXAFS distances for $[Fe^{IV}$═$O(TMC)(CH_3CN)]^{2+}$ gave first shell bond lengths of 1.63 and 2.09 Å for the Fe═O bond and the Fe−N

dx.doi.org/10.1021/ja3046298 | J. Am. Chem. Soc. 2012, 134, 11791−11806

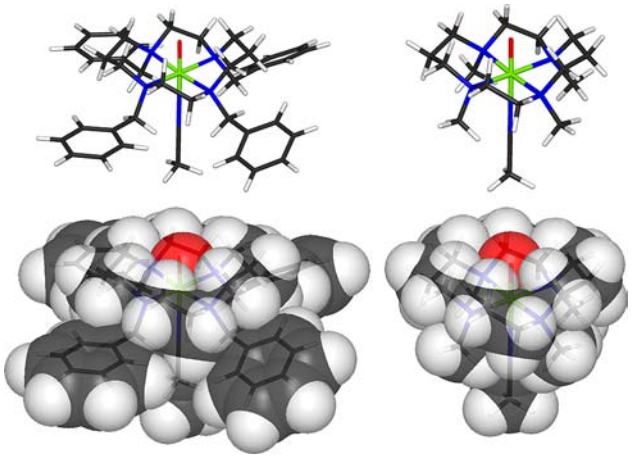

Figure 6. Final geometry optimized model for **2** used in conjunction with fitting the EXAFS data. Space filling models of **2** (left) compared with $[Fe^{IV}{=}O(TMC)(CH_3CN)]^{2+}$ (right) show increased steric interactions between the benzyl groups and with the cyclam ring. These interactions result in a greater distortion at the iron and a smaller oxo cage.

coordination of the TMC ligand and axial acetonitrile (Table 2). As was found for the EXAFS data on **1** and **2**, the outer shell of $[Fe^{IV}{=}O(TMC)(CH_3CN)]^{2+}$ could also be fit well using either MS paths from TMC or the intense forward focused MS from the axial CH_3CN, but not both simultaneously, as the two paths are not individually resolvable given the overlap of the EXAFS waves and k range of the data. The EXAFS of **2** and $[Fe^{IV}{=}O(TMC)(CH_3CN)]^{2+}$ are very similar, with the most notable difference being the consistently larger bond variance values across most paths of **2**, implying a more disordered metal site. The exception to this is the bond variance of the Fe=O path which is roughly ~100 Å^2 less for **2** relative to $[Fe^{IV}{=}O(TMC)(CH_3CN)]^{2+}$. This indicates that **2** has a more constrained Fe=O unit, suggesting a smaller oxo-cage or a stronger Fe=O bond relative $[Fe^{IV}{=}O(TMC)(CH_3CN)]^{2+}$. These differences are also consistent with the more intense pre-edge discussed above.

3.3. Reactivity of $[Fe^{IV}{=}O(TBC)(CH_3CN)]^{2+}$. The reactivity of **2** was first investigated for its activation of an H-atom from ethylbenzene, where an H-atom is abstracted from the benzylic position,[16] and gave a second-order rate constant of 1.5(2) × 10^{-2} M^{-1} s^{-1}. Using deuterated ethylbenzene-d_{10}, a large kinetic isotope effect (KIE) with a value of 17 was also determined (SI Figure 9); a value similar to those observed in the oxidation of ethylbenzene by other nonheme iron(IV)−oxo complexes.[14,70] This indicates that the C−H bond activation of ethylbenzene is involved in the rate-determining step in the oxidation reaction of ethylbenzene by **2**. For comparison, the reactivities of $[Fe^{IV}{=}O(N4Py)]^{2+}$ and $[Fe^{IV}{=}O(TMC)(CH_3CN)]^{2+}$ were also investigated and yielded a second-order rate constant of 1.3(2) × 10^{-3} M^{-1} s^{-1} for $[Fe^{IV}{=}O(N4Py)]^{2+}$, while in the case of $[Fe^{IV}{=}O(TMC)(CH_3CN)]^{2+}$, very little reactivity was observed, with the upper limit determined as < 9.6 × 10^{-5} M^{-1} s^{-1} (Figure 7A). These results indicate that **2** is 10 times more reactive than $[Fe^{IV}{=}O(N4Py)]^{2+}$ and 2 orders of magnitude larger than $[Fe^{IV}{=}O(TMC)(CH_3CN]^{2+}$ in the oxidation of ethylbenzene.

Second, the oxo-transfer reactivity of **2** was investigated using thioanisole derivatives, where upon addition of thioanisole (10 mM) to a solution of **2** (0.50 mM), the oxo group was

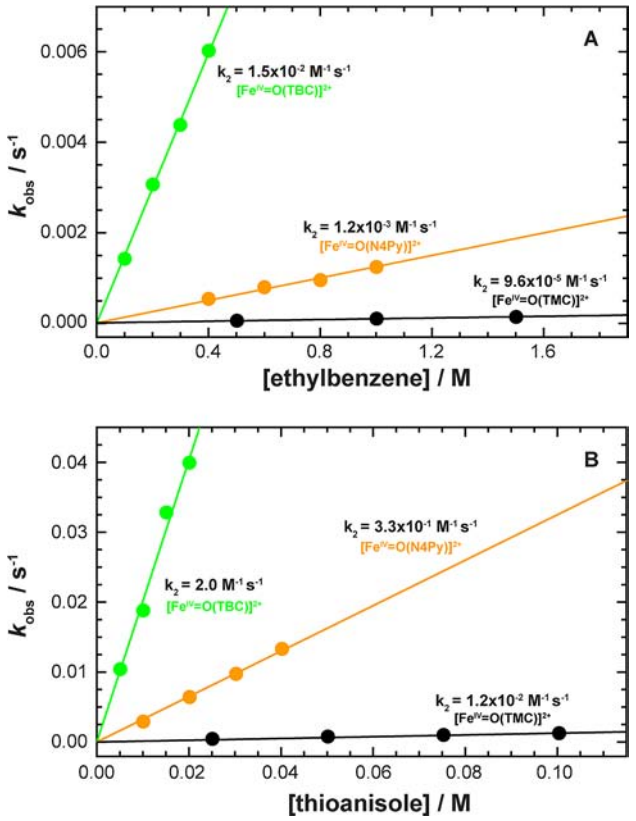

Figure 7. Observed reaction rates and second-order rate constants for **2** compared to other known nonheme $Fe^{IV}{=}O$ models. (A) k_{obs} vs the concentration of ethylbenzene in H-atom abstraction reactions. (B) k_{obs} vs the concentration of thioanisole in oxo-transfer reactions. $[Fe^{IV}{=}O(TBC)(CH_3CN)]^{2+}$ (**2**) (green), $[Fe^{IV}{=}O(N4Py)]^{2+}$ (orange), and $[Fe^{IV}{=}O(TMC)(CH_3CN)]^{2+}$ (black).

successfully transferred from the $Fe^{IV}{=}O$ to the substrate, and the intermediate quantitatively converted back to the starting ferrous complex, yielding methyl phenyl sulfoxide (SI Figure 10). Pseudo-first-order rate constants determined by fitting the kinetic data for the decay of **2** increased linearly with substrate concentration and yielded a second-order rate constant of 2.0(2) M^{-1} s^{-1} (SI Figure 11A). Pseudo-first-order rate constants were also determined using various *para*-substituted thioanisoles and plotted against σ_p, enabling the determination of a Hammett value ρ = −2.3 (SI Figure 11B). The negative ρ value indicates both the electrophilic character of the oxo group in the nonheme $Fe^{IV}{=}O$ complexes and a positive charge buildup on sulfur in sulfoxidation reactions.[73] The reactivities of $[Fe^{IV}{=}O(N4Py)]^{2+}$ and $[Fe^{IV}{=}O(TMC)(CH_3CN)]^{2+}$were also investigated with thioanisole and afforded second-order rate constants with a reactivity order of $[Fe^{IV}{=}O(TBC)]^{2+}$ > $[Fe^{IV}{=}O(N4Py)]^{2+}$ > $[Fe^{IV}{=}O(TMC)(CH_3CN)]^{2+}$ (Figure 7B); again a more than 2 orders of magnitude increase from 1.2 × 10^{-2} to 2.0 M^{-1} s^{-1} for $[Fe^{IV}{=}O(TMC)(CH_3CN)]^{2+}$ and **2**, respectively.

4. DFT CALCULATIONS

In order to understand the observed reactivity differences between $[Fe^{IV}{=}O(TBC)(CH_3CN)]^{2+}$ (**2**) and $[Fe^{IV}{=}O(TMC)(CH_3CN)]^{2+}$, a series of DFT calculations were conducted for both H-atom abstraction and oxo-transfer reactions. A table comparing the effects of functional, basis set, and solvent on the final energy splitting between the

dx.doi.org/10.1021/ja3046298 | J. Am. Chem. Soc. 2012, 134, 11791−11806

Table 4. Key Bond Distances and Angles for S = 1 and 2 for Fe^{IV}=O Complexes[a]

	$[Fe^{IV}=O(TBC)(CH_3CN)]^{2+}$ (2)			$[Fe^{IV}=O(TMC)(CH_3CN)]^{2+}$		
bond distance/angle	S = 1	S = 2	Δ	S = 1	S = 2	Δ
Fe=O	1.61	1.61	0.00	1.62	1.61	0.00
Fe−N CH_3CN	2.12	2.09	−0.04	2.12	2.08	−0.04
average Fe−N TXC	2.15	2.24	0.09	2.14	2.22	0.08
Fe−N plane	−0.06	−0.08	−0.02	−0.05	−0.08	−0.03
O−H plane	−0.38	−0.40	−0.02	−0.37	−0.39	−0.03
average O−H crown	2.37	2.39	0.02	2.41	2.43	0.02
Fe−N standard deviation	0.03	0.07	0.05	0.01	0.06	0.06
∠O−Fe−TXC	88.32	87.93	−0.39	88.70	88.16	−0.54
∠TXC−Fe−CH_3CN	91.69	92.10	0.41	91.32	91.88	0.56
∠equatorial standard deviation	6.38	7.79	1.41	6.05	6.45	0.40

[a]Geometric parameters for S = 1 and 2 ground and excited states, respectively, for $[Fe^{IV}=O(TBC)(CH_3CN)]^{2+}$ (2) and $[Fe^{IV}=O(TMC)(CH_3CN)]^{2+}$. Structures calculated using B3LYP/6-311G(d). All distances are given in Å, all angles (∠) are in degrees. A more extensive table is reproduced in SI Table 4.

ground and excited states for Fe^{II} and Fe^{IV}=O TBC and TMC is provided in SI Table 3.

As a calibration, DFT calculations were first performed on the known system $[Fe^{IV}=O(TMC)(CH_3CN)]^{2+}$, with an S = 1 ground state, as both a single point on the crystal structure (CSD 192768)[18] and as a fully optimized geometry. Geometry optimization did not appreciably change the structure from that of the crystallography, calculating the Fe=O bond at ∼1.61 Å, the equatorial iron−nitrogen TMC distances at an average of ∼2.13 Å, and the axial acetonitrile at 2.12 Å (Table 4 and SI Table 4 with SI Figure 12 as reference). In all cases, values for orbital energies and covalencies agreed well with previous calculations on this system.[39]

As crystallographic data are not currently available for $[Fe^{IV}=O(TBC)(CH_3CN)]^{2+}$, a low-spin S = 1 geometry was calculated based on the above spectroscopic characterizations. An initial starting geometric structure was constructed based on a similar nickel-containing TBC complex $[Ni^{II}(TBC)(Cl)]^{+}$ by changing the Ni^{II} to an Fe^{IV}, adding an oxo and acetonitrile group in the trans-axial position, and optimizing the geometry. To ensure the correct conformation of $[Fe^{IV}=O(TBC)(CH_3CN)]^{2+}$, the structure was evaluated by interchanging the oxo and axial acetonitrile groups from oxo-*anti* to oxo-*syn* relative to the benzyl groups. Comparison of the final energies of the reoptimized conformations indicated that the conformation with oxo *anti* to the benzyl groups was energetically favorable by ∼3.2 kcal/mol (SI Table 5). As a calibration, these results were compared with the crystallographic data on $[Fe^{IV}=O(TMC)(CH_3CN)]^{2+}$, where the oxo is defined to be orientated *anti* to the methyl groups. The calculations for $[Fe^{IV}=O(TMC)(CH_3CN)]^{2+}$ also show that the *syn* conformation is energetically unfavorable by ∼4.0 kcal/mol.

4.1. Comparison of Fe^{IV}=O TBC to TMC. A direct comparison of the geometry optimized models of $[Fe^{IV}=O(TBC)(CH_3CN)]^{2+}$ and $[Fe^{IV}=O(TMC)(CH_3CN)]^{2+}$ in the S = 1 ground state reveals several small but significant differences. In $[Fe^{IV}=O(TBC)(CH_3CN)]^{2+}$, the substitution of benzyl groups on the cyclam ligand adds an appreciable amount of steric bulk next to the axial acetonitrile over the methyl groups in $[Fe^{IV}=O(TMC)(CH_3CN)]^{2+}$. This leads to twists and tilts of the benzyl rings and a slight folding of the cyclam ring, decreasing the cavity for the oxo group, as the bottom portion of the complex is splayed out to accommodate the increased steric bulk (Figure 6). From the optimized geometries, this substitution also results in slightly longer equatorial Fe−N bond lengths, a tighter hydrogen−oxo cage (average O−H crown), an iron that is farther below the nitrogen equatorial plane (Table 4, Fe N-plane, more acute ∠O−Fe−TBC, and more obtuse ∠TBC−Fe−CH_3CN angles), and an overall more distorted complex, evident by the 3-fold larger standard deviation (SD) in the equatorial bond lengths as well as by the increased SD in the ∠N−Fe−N equatorial angles (Table 4, Fe^{IV}=O TBC and TMC S = 1).

These calculations reproduce the differences between $[Fe^{IV}=O(TBC)(CH_3CN)]^{2+}$ and $[Fe^{IV}=O(TMC)(CH_3CN)]^{2+}$ that were observed in the EXAFS data, where the fits of $[Fe^{IV}=O(TBC)(CH_3CN)]^{2+}$ show both slightly longer Fe−N bonds and a larger degree of bond variance, indicating a more distorted metal environment (fit 2-1 vs 3-1, Table 2). These calculations also reproduced the intensity difference observed in the pre-edge data between $[Fe^{IV}=O(TBC)(CH_3CN)]^{2+}$ and $[Fe^{IV}=O(TMC)(CH_3CN)]^{2+}$ (33.7 and 30.0 normalized units, respectively), as these gave a total metal 4p mixing of 29.8% for $[Fe^{IV}=O(TBC)(CH_3CN)]^{2+}$ and 24.5% for $[Fe^{IV}=O(TMC)(CH_3CN)]^{2+}$. Based on previously determined values[56] where 1% metal 4p character corresponds to ∼1.22 (0.5) units of pre-edge intensity, the calculations (including the quadrupole contribution from the d character) predict pre-edge intensities of 36 and 29 units for $[Fe^{IV}=O(TBC)(CH_3CN)]^{2+}$ and $[Fe^{IV}=O(TMC)(CH_3CN)]^{2+}$, respectively; a result consistent with the greater structural distortion reflected in the larger EXAFS bond variances and the larger calculated displacement of the iron from the equatorial nitrogen plane, further calibrating the DFT calculations to the experiment.

Based on the spectroscopic differences observed experimentally and the insight gained through the geometry optimized structures showing that the Fe=O unit is more constrained in the cyclam for $[Fe^{IV}=O(TBC)(CH_3CN)]^{2+}$ relative to $[Fe^{IV}=O(TMC)(CH_3CN)]^{2+}$, an even lower rate of reaction would be expected. However, this is in contrast to the reactivity studies (vide supra) where $[Fe^{IV}=O(TBC)(CH_3CN)]^{2+}$ exhibited rate constants that are 2 orders of magnitude larger than those measured for $[Fe^{IV}=O(TMC)(CH_3CN)]^{2+}$.

The structures of $[Fe^{IV}=O(TBC)(CH_3CN)]^{2+}$ and $[Fe^{IV}=O(TMC)(CH_3CN)]^{2+}$ were therefore also optimized for the S = 2 excited states. These calculations revealed that the energetic gap between S = 1 and 2 is smaller by ∼3.2 kcal/mol for $[Fe^{IV}=O(TBC)(CH_3CN)]^{2+}$ relative to $[Fe^{IV}=O(TMC)(CH_3CN)]^{2+}$ (Table 5, ΔG(solvent), B3LYP), as the more

dx.doi.org/10.1021/ja3046298 | J. Am. Chem. Soc. 2012, 134, 11791−11806

Table 5. Calculated Energy Differences: Fe^{IV}=O S = 2 Excited State Relative to S = 1 Ground State[a]

	$[Fe^{IV}$=O(TBC)$(CH_3CN)]^{2+}$ (**2**)		$[Fe^{IV}$=O(TMC)$(CH_3CN)]^{2+}$	
	B3LYP	BP86	B3LYP	BP86
$\Delta\varepsilon$(gas)	3.2	13.5	4.9	15.0
$\Delta\varepsilon$(solvent)	2.7	13.0	5.8	16.1
ΔE(solvent)	1.0	11.2	3.9	14.1
ΔH(solvent)	1.4	11.7	4.5	14.8
ΔG(solvent)	−0.3	9.7	2.9	12.7

[a]All values in kcal/mol, calculated for just Fe^{IV}=O TBC and TMC; $\Delta\varepsilon$(gas) G03/6-311+G(2df,2pd) without ZPE; ΔE(solvent) with ZPE correction and solvent (acetonitrile). Geometry optimization done using G03/B3LYP or BP86/6-311G(d).

distorted ligand environment caused by the steric interaction of the benzyl rings (Figure 6) weakens the equatorial and axial ligand field, stabilizing the $d_{x^2-y^2}$ and d_{z^2} orbitals. This is consistent with the measurably larger D value defined for $[Fe^{IV}$=O(TBC)$(CH_3CN)]^{2+}$ (29.5 cm^{-1}) relative to $[Fe^{IV}$=O(TBC)$(CH_3CN)]^{2+}$ (28 cm^{-1}), Table 3.[17,18,28] The lower energy of the S = 2 excited state for $[Fe^{IV}$=O(TBC)$(CH_3CN)]^{2+}$ provides a pathway for its increased reactivity (vide infra).

4.2. H-Atom Abstraction. A set of two reaction coordinates were calculated for both $[Fe^{IV}$=O(TBC)$(CH_3CN)]^{2+}$ and $[Fe^{IV}$=O(TMC)$(CH_3CN)]^{2+}$, starting from the experimentally determined S = 1 ground state utilizing ethylbenzene. (Reaction coordinate diagram for ΔG(solvent) in Figure 8). ΔE(solvent) in SI Figure 13. Select geometric parameters are available in Table 6 with additional values in SI Table 6.) As observed in previous studies,[4,39,40] an electrophilic attack by a low-spin Fe^{IV}=O species is enabled through a π-attack of the oxo $p_{x/y}$ FMO. This leads to the transfer of a H-atom along with a single β-spin electron from the highest occupied molecular orbital (HOMO) of the substrate into the $d_{xz/yz}$ π^* orbital of the iron to generate a low-spin ferric product and a radical on the substrate (Figure 9, top). Since the electron is transferred into the π set of iron d orbitals, this requires a side-on approach of the C−H bond of the substrate relative to the Fe=O to ensure good orbital overlap. In the case of a sterically hindered cyclam ligand, this results in a very large transition state barrier. For both $[Fe^{IV}$=O(TBC)$(CH_3CN)]^{2+}$ and $[Fe^{IV}$=O(TMC)$(CH_3CN)]^{2+}$, the transition state has an Fe−O−substrate angle of ∼144° and calculated barrier heights of $\Delta G^{\ddagger}$ = 24.7 and 25.0 kcal/mol, with that for $[Fe^{IV}$=O(TBC)$(CH_3CN)]^{2+}$ slightly higher due to its more constrained oxo-cage (Figure 8, S = 1 TS). Barrier heights of this magnitude are too large to correlate with the observed H-atom reactivity of $[Fe^{IV}$=O(TBC)$(CH_3CN)]^{2+}$. In addition, the low-spin ferric products of this reaction are calculated to be endergonic by around ∼4 kcal/mol. Therefore, reactivity on the S = 1 surface is not feasible for an Fe^{IV}=O unit with the sterically hindered cyclam ligand, and reaction coordinates were evaluated for each complex on the S = 2 surface.

In contrast to the π-attack required by the side-on approach for the low-spin complex, H-atom abstraction by an S = 2 Fe^{IV}=O complex to form a high-spin ferric product involves a σ-attack and the transfer of an α-spin electron from the HOMO of the substrate into the unoccupied d_{z^2} σ^* orbital on the iron (Figure 9, bottom). As the d_{z^2} is σ antibonding with the oxo p_z

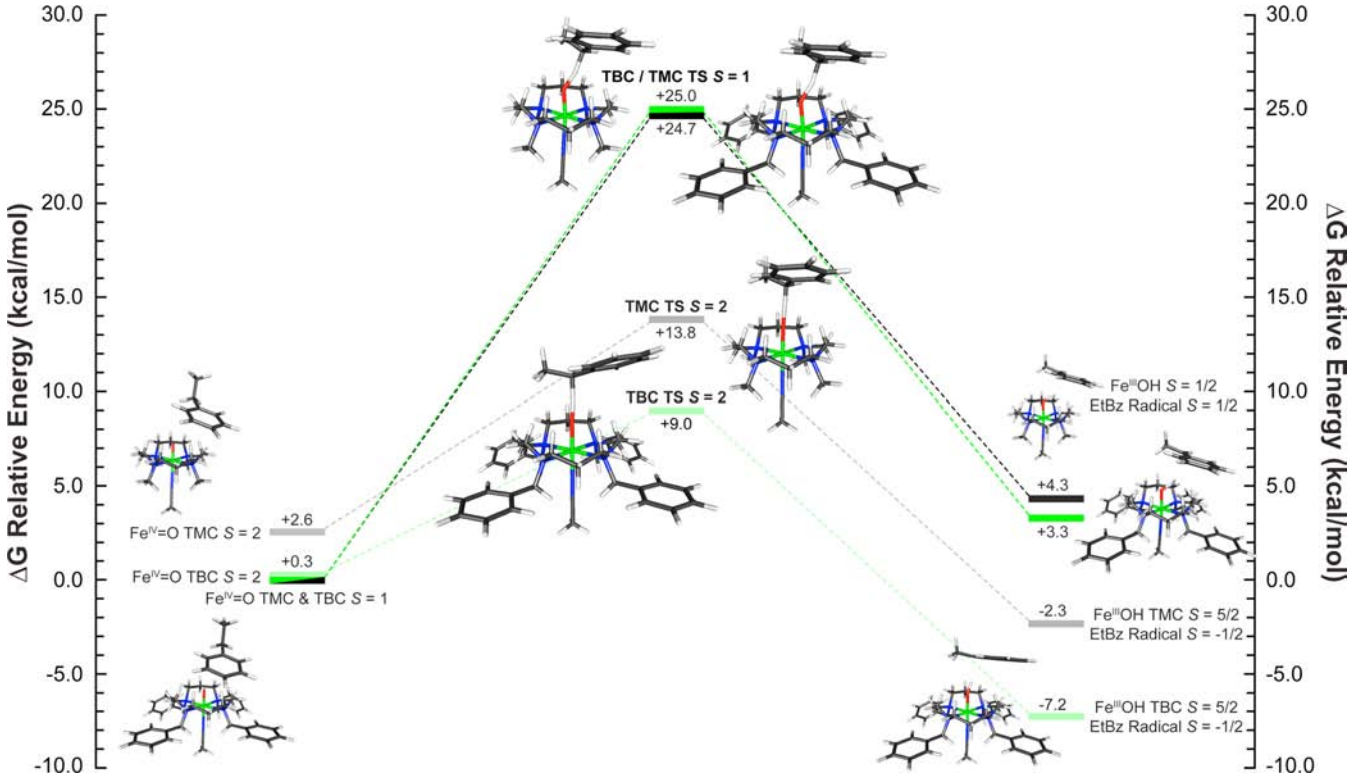

Figure 8. H-atom abstraction reaction coordinate of $[Fe^{IV}$=O(TBC)$(CH_3CN)]^{2+}$ (S = 1 green, S = 2 light-green) and $[Fe^{IV}$=O(TMC)$(CH_3CN)]^{2+}$ (S = 1 black, S = 2 gray) with ethylbenzene. Energies given for ΔG(solvent = acetonitrile) in units of kcal/mol, with the S = 1 ground state of each series defined as 0.0 kcal/mol.

dx.doi.org/10.1021/ja3046298 | J. Am. Chem. Soc. 2012, 134, 11791−11806

Table 6. Geometric Parameters for 2 and $[Fe^{IV}{=}O(TMC)(CH_3CN]^{2+}$ for H-atom Transfer and Oxo-Transfer Transition State Complexes[a]

	$[Fe^{IV}{=}O(TBC)(CH_3CN)]^{2+}$ (2)						$[Fe^{IV}{=}O(TMC)(CH_3CN)]^{2+}$					
	GS/ES		H-atom transfer		oxo-transfer		GS/ES		H-atom transfer		oxo-transfer	
measurement	S = 1	S = 2	S = 1	S = 2	S = 1	S = 2	S = 1	S = 2	S = 1	S = 2	S = 1	S = 2
oxo-H/S (H−C)	–	–	1.27(1.34)	1.25(1.34)	2.03	2.07	–	–	1.28(1.33)	1.42(1.23)	1.92	2.07
Fe=oxo	1.61	1.61	1.75	1.76	1.87	1.78	1.62	1.61	1.75	1.73	1.86	1.80
Fe−N CH_3CN	2.12	2.09	2.10	2.36	2.30	4.08	2.12	2.08	2.09	2.32	2.28	2.51
av. Fe−N eq.	2.15	2.24	2.16	2.25	2.17	2.21	2.14	2.22	2.13	2.23	2.16	2.23
Fe out of plane	−0.06	−0.08	−0.03	0.05	0.01	0.34	−0.05	−0.07	−0.02	0.05	0.04	0.13
O−H plane dist.	−0.38	−0.40	−0.21	−0.11	−0.04	0.23	−0.37	−0.39	−0.20	−0.14	−0.01	0.03
av. O−H dist.	2.37	2.39	2.39	2.41	2.42	2.55	2.41	2.43	2.43	2.45	2.51	2.51
Fe−N shell SD	0.03	0.07	0.04	0.06	0.07	0.84	0.01	0.06	0.03	0.04	0.06	0.13
∠Fe−O−sub.	–	–	144.04	176.45	153.07	154.84	–	–	143.64	176.12	148.98	153.46
$\angle\theta$ (horiz. to O $P_{x/y}$)	–	–	61.24	86.28	44.79	34.57	–	–	60.75	86.57	52.23	40.79
Δ (horiz. offset O P_z)	–	–	1.24	0.17	0.92	0.88	–	–	1.26	0.16	0.99	0.93
H-plane−sub. dist.	–	–	2.14	2.47	1.85	2.15	–	–	2.15	2.51	1.75	1.95

[a]Geometric parameters for the S = 1 ground state (GS) and the S = 2 excited state (ES) reproduced from Table 4 along with those of the corresponding H-atom abstraction and oxo-transfer transition state complexes of $[Fe^{IV}{=}O(TBC)(CH_3CN)]^{2+}$ (**2**) and $[Fe^{IV}{=}O(TMC)(CH_3CN)]^{2+}$. Structures calculated using B3LYP/6-311G(d). All distances are given in Å, all angles (∠) are in degrees. SD = standard deviation, av. = average, eq. = equatorial, dist. = distance, sub. = substrate, horiz. = horizontal. Reference SI Figure 12 for descriptions and SI Tables 4, 6, and 7 for additional parameters.

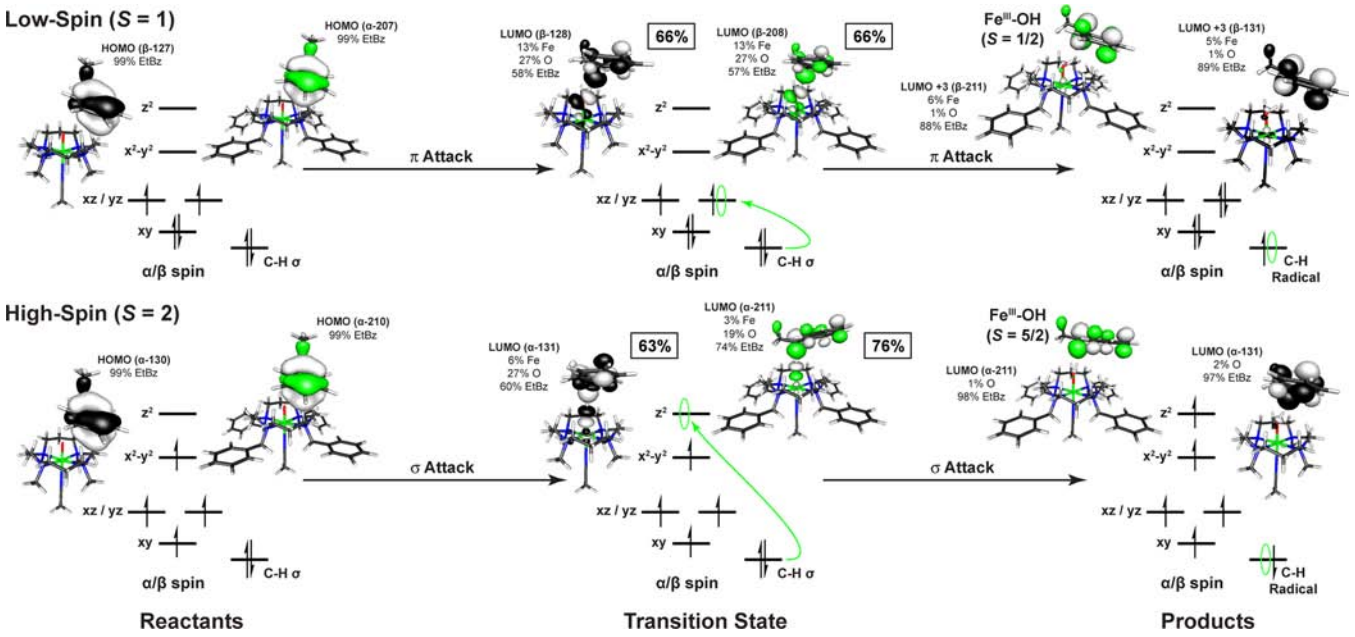

Figure 9. Comparison of low-spin and high-spin FMOs involved in the H-atom transfer reaction for $[Fe^{IV}{=}O(TBC)(CH_3CN)]^{2+}$ (green) and $[Fe^{IV}{=}O(TMC)(CH_3CN)]^{2+}$ (black) with ethylbenzene.

orbital, good orbital overlap will result from an end-on approach of the substrate, as is observed in the transition state, with the Fe−O−H−C (substrate) bond angle now close to linear (~176°) for both complexes (Figure 8 S = 2 TS, Table 6). The end-on approach of the substrate substantially lowers the barrier to reactivity by decreasing the substrate−cyclam steric interaction, yielding reduced barrier heights of $\Delta G^{\ddagger}$ = 13.8 and 9.0 kcal/mol (ΔG(solvent = acetonitrile), B3LYP) for $[Fe^{IV}{=}O(TMC)(CH_3CN)]^{2+}$ and $[Fe^{IV}{=}O(TBC)(CH_3CN)]^{2+}$, respectively. This difference in the calculated transition state barrier height for the two complexes is now 4.8 kcal/mol, with $[Fe^{IV}{=}O(TBC)(CH_3CN)]^{2+}$ lower; a result that is comparable to the observed > 10^2 rate increase of H-atom reactivity by $[Fe^{IV}{=}O(TBC)(CH_3CN)]^{2+}$.

It is important to note that the energetic gap between the S = 1 and 2 states in the complete reactant complex (substrate included) is smaller by 2.3 kcal/mol for $[Fe^{IV}{=}O(TBC)(CH_3CN)]^{2+}$ relative to $[Fe^{IV}{=}O(TMC)(CH_3CN)]^{2+}$ (Figure 8). This difference, which was due to the weaker ligand field $[Fe^{IV}{=}O(TBC)(CH_3CN)]^{2+}$, becomes even larger at the transition state ($\Delta\Delta G^{\ddagger}$ = 4.8 kcal/mol), as the transfer of an electron into the d_z^2 orbital combined with the steric bulk of the benzyl substituents elongates the trans-axial CH_3CN bond allowing greater out-of-plane movement of the iron, a longer Fe=O bond, and a more exposed oxo which is now just below the cyclam hydrogen crown (SI Figure 12). These changes further lower the steric contribution to the barrier for $[Fe^{IV}{=}$

dx.doi.org/10.1021/ja3046298 | J. Am. Chem. Soc. 2012, 134, 11791−11806

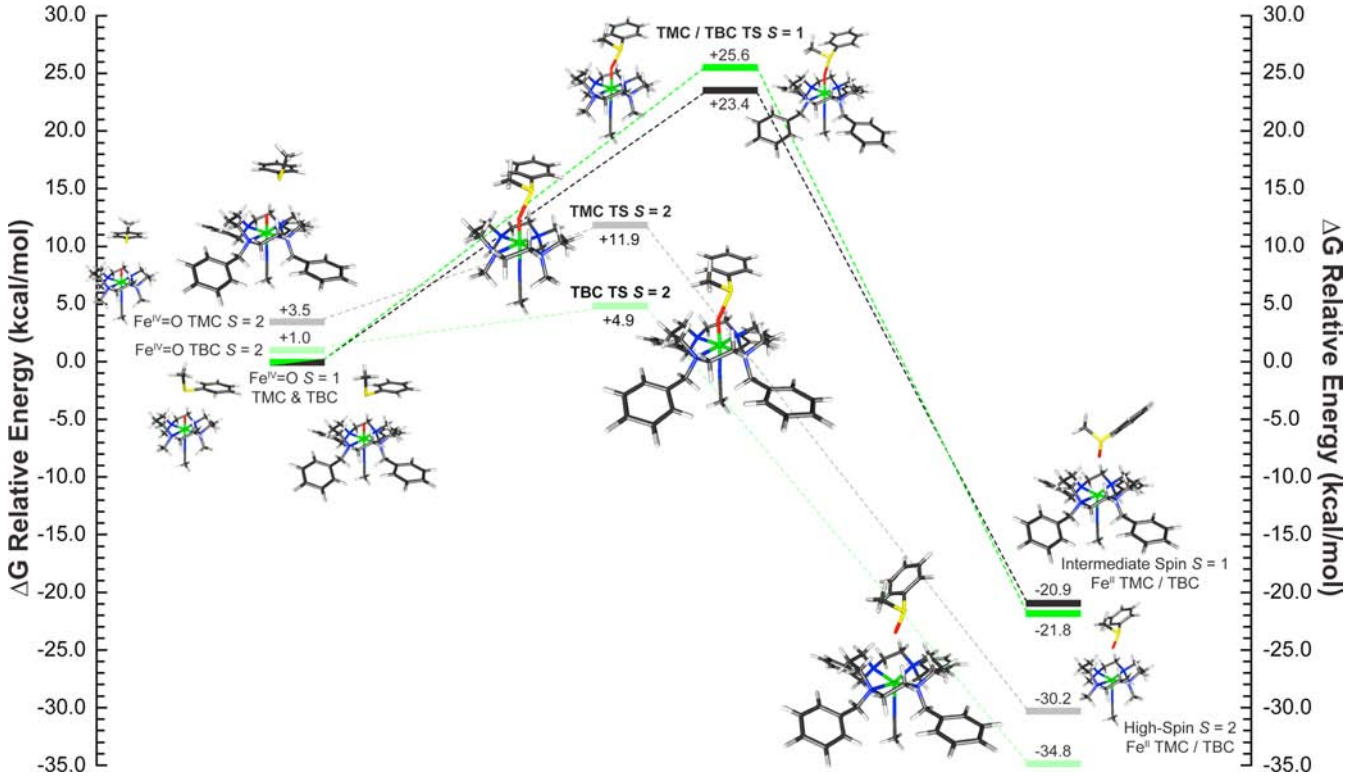

Figure 10. Oxo-transfer reaction coordinate of $[Fe^{IV}{=}O(TBC)(CH_3CN)]^{2+}$ (S = 1 green, S = 2 light-green) and $[Fe^{IV}{=}O(TMC)(CH_3CN)]^{2+}$ (S = 1 black, S = 2 gray) with thioanisole. Energies given for ΔG(solvent = acetonitrile) in units of kcal/mol, with the S = 1 ground state of each series defined as 0.0 kcal/mol. Transition states have been shifted right/left of center, based on the lengths of the Fe=O bond, to indicate reaction progress (Table 6).

$O(TBC)(CH_3CN)]^{2+}$ and yield the faster rate of H-atom abstraction.

4.3. Oxo-Transfer Reactivity. To correlate with the reactivity data and elucidate the differences between H-atom abstraction and oxo-transfer reactions, S = 1 and 2 transition states and IRCs were calculated for the reaction coordinate of thioanisole with Fe^{IV}=O TBC and TMC (Figure 10 and SI Figure 14). Energetically, oxo-transfer parallels H-atom abstraction with the S = 1 surface having unreasonably large transition state barriers ($\Delta G^{\ddagger}$ = 25.0 and 24.7 kcal/mol) and the S = 2 surface having a lower barrier for $[Fe^{IV}{=}O(TBC)(CH_3CN)]^{2+}$ relative to $[Fe^{IV}{=}O(TMC)(CH_3CN)]^{2+}$ (9.0 vs 13.8 kcal/mol). While the energy differences for H-atom abstraction could be accounted for by the relative orientations of substrate approach required by the FMOs (~150° vs 176° relative to the Fe=O bond), in the oxo-transfer transition state, the substrate approaches with an angle of ~150° for both complexes in both spin states (Table 6 and SI Table 7). This is due to the fact that in contrast to a H-atom abstraction reaction, which is a one-electron process, the sulfoxidation reaction is a two-electron process, which results in the formation of a ferrous product complex. As such, regardless of spin state, the two-electron transfer requires that the donor orbital of the substrate achieves both π and σ overlap with the sterically shielded oxo group. Therefore, the critical angle is not the Fe−O−substrate angle, as in H-atom abstraction, but the orientation of the donor orbital of the substrate relative to the oxo p_z and $p_{x/y}$ FMOs. For thioanisole, the DFT calculations define the substrate FMO as the sulfur b_1, which is oriented perpendicular to the CH_3−S−Ph plane and transfers two electrons, one α and one β, into the iron d_z^2 σ^* and $d_{xz/yz}$ π^* orbitals, respectively. As such, the tilt (θ) and horizontal offset (Δ) of the b_1 orbital relative to the oxygen $p_{x/y}$ and p_z orbitals will affect its ability to overlap with these FMOs of the Fe^{IV}=O group (Figure 11).

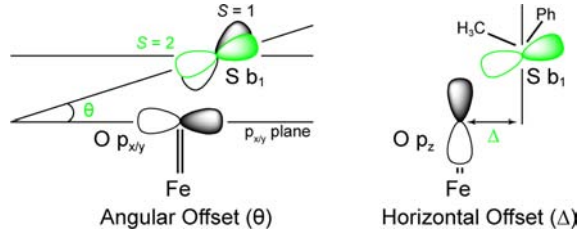

Figure 11. Orbital diagram illustrating how the angular offset θ (left, oxo $p_{x/y}$ plane set to 0°) and the horizontal offset Δ (right, oxo p_z axis set to 0) affects the ability of the sulfur b_1 to maintain orbital overlap with the oxygen $p_{x/y}$ and p_z to transfer both the β (π) and α (σ) electrons to the iron $d_{xz/yz}$ and d_z^2 orbitals, respectively; S = 1 (black), S = 2 (green).

On the S = 1 surface, the unoccupied d_z^2 orbital on the iron is high in energy due to the strong Fe=O bond, and thus only $d_{xz/yz}$ orbital is available for π-attack. From the DFT calculations, π-attack of the sulfur b_1 FMO on the sterically hindered $d_{xz/yz}$ orbitals results in a significant elongation of the Fe=O bond (1.61 to 1.87 Å, for both complexes, Table 6), a smaller cyclam−substrate distance (H-plane−substrate distance ~1.8 Å), and a large steric contribution to the S = 1 transition state barrier (~25 kcal/mol) (Figure 10). This cyclam−substrate steric interaction produces a b_1 angle θ of ~48.5° relative to the oxo $p_{x/y}$ orbital plane and limited overlap between the sulfur b_1 and oxo $p_{x/y}$ FMOs. However, as the β

dx.doi.org/10.1021/ja3046298 | J. Am. Chem. Soc. 2012, 134, 11791−11806

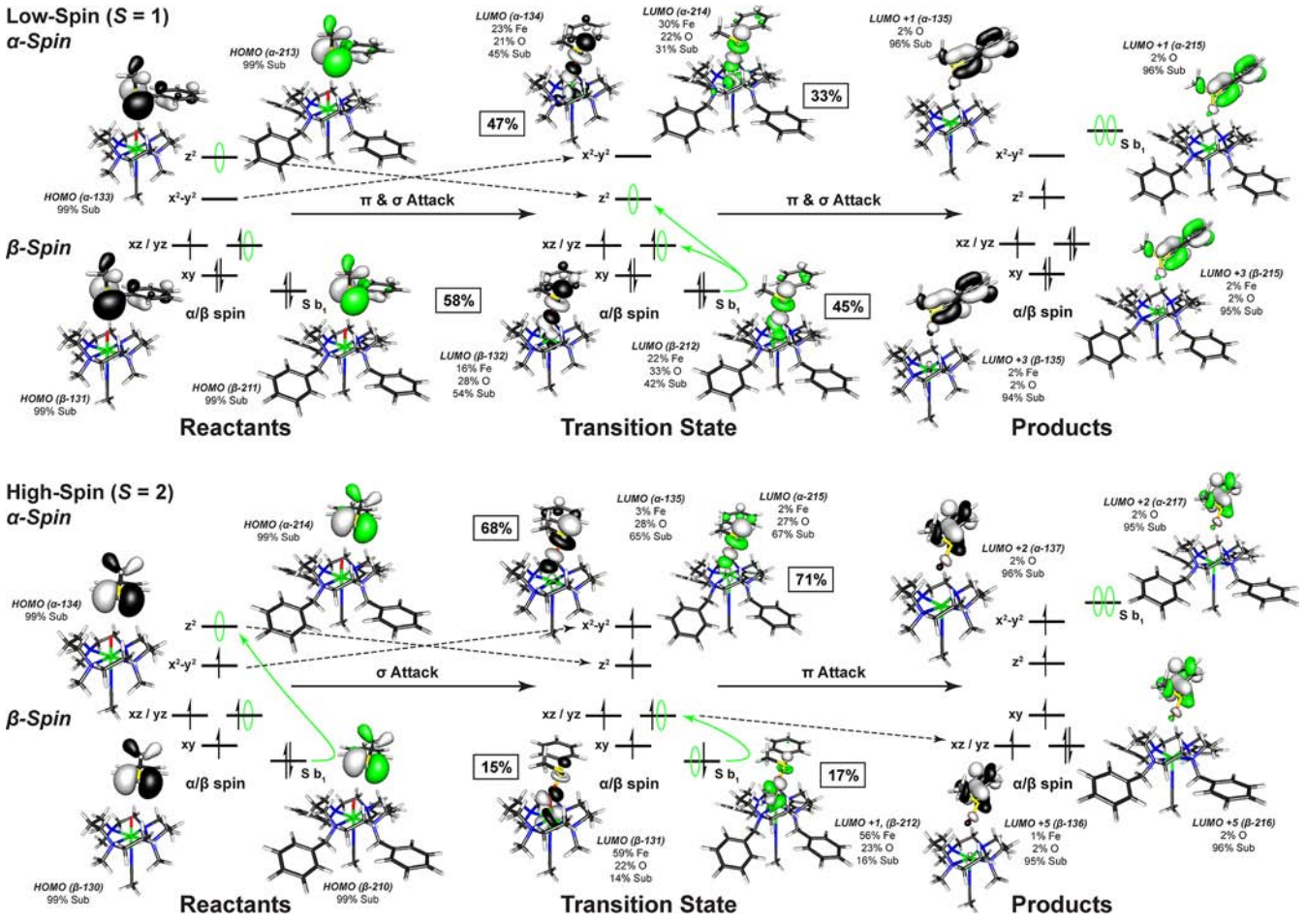

Figure 12. Comparison of low-spin and high-spin FMOs involved in the oxo-transfer reaction for $[Fe^{IV}{=}O(TBC)(CH_3CN)]^{2+}$ (green) and $[Fe^{IV}{=}O(TMC)(CH_3CN)]^{2+}$ (black) with thioanisole. From the $S = 1$ ground state, both electrons are transferred in a concerted process at similar rates. On the $S = 2$ surface, the electrons are transferred sequentially through a high-spin ferric transition state. The percent of electron transfer is given next to each transition state complex and in SI Table 8.

electron transfers, the Fe=O bond elongates and stabilizes the d_z^2 orbital making it accessible for the transfer of the second (α) electron. This yields an almost concerted electron transfer for the $S = 1$ surface, with ~52% β vs ~40% α electron transferred at the TS (Figure 12 (top), SI Table 8).

On the $S = 2$ surface, the α d_z^2 orbital is low in energy, and the exposed oxo p_z orbital allows for direct σ-attack and results in the transfer of a single α electron from the sulfur b_1 to the iron d_z^2 σ^* orbital early in the reaction coordinate (~70% α-spin relative to ~16% β transferred at the TS) (Figure 12 (bottom), SI Table 8). This sequential electron transfer leads to a high-spin ferric transition state where the addition of the α electron into the iron d_z^2 orbital weakens both the Fe=O and the trans-axial iron−acetonitrile bond. As a result of their high-spin ferric character, the $S = 2$ transition states also have longer Fe−N equatorial bonds, which in combination with the weaker trans-axial acetonitrile allows for greater out-of-plane displacement of the iron and more flexibility for the cyclam ring to distort and expose the oxo group, which is now above the plane of the cyclam hydrogen crown (O−H plane distance, Table 6).

An overlay of the $S = 1$ vs 2 transition states for the two complexes reveals that the high-spin transition states have a less sterically hindered oxo-cage and a greater cyclam−substrate distance (Figure 13), as reflected in the average O−H distance and the H-plane−substrate distance (Table 5). These structural

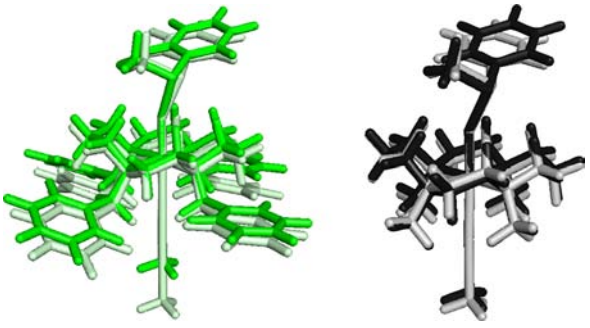

Figure 13. Overlay of the oxo-transfer transition state geometries for $[Fe^{IV}{=}O(TBC)(CH_3CN)]^{2+}$ $S = 1$ (green) and $S = 2$ (light-green) and $[Fe^{IV}{=}O(TMC)(CH_3CN)]^{2+}$ $S = 1$ (black) and $S = 2$ (gray).

changes for the $S = 2$ states allow the sulfur b_1 FMO to adopt a smaller angle θ of 34.6° relative to the oxo $p_{x/y}$ plane (Figure 11) at the transition state that results in better overlap. These geometric changes facilitate the transfer of the second (β) electron without an additional contribution to the barrier.

As with H-atom abstraction, the ~7 kcal/mol difference at the transition state between $[Fe^{IV}{=}O(TBC)(CH_3CN)]^{2+}$ and $[Fe^{IV}{=}O(TMC)(CH_3CN)]^{2+}$ on the $S = 2$ surface reflects the additional effects of the TBC ligand; the largest of which is that the axial acetonitrile bond is now 4.08 Å (vs 2.51 Å in TMC,

dx.doi.org/10.1021/ja3046298 | J. Am. Chem. Soc. 2012, 134, 11791−11806

Table 6). With the axial ligand displaced by the bulk of the benzyl groups, the iron center is 5-coordinate, which results in a larger out-of-plane displacement (0.34 vs 0.13 Å) and a greater flexibility for the cyclam ring to expose the oxo group (0.23 vs 0.03 Å for Fe^{IV}=O TBC and TMC, respectively, Table 6 and SI Figure 13). These changes allow for better accessibility of the substrate and greater orbital overlap at a long cyclam−substrate distance (2.15 Å for TBC vs 1.95 Å for TMC, Table 6) and therefore result in the lowest barrier for oxo-transfer.

5. DISCUSSION

The TBC ligand is a simple derivative of TMC where four benzyl groups have replaced the methyl groups, resulting in greater cyclam strain and steric interactions between these groups. Fe^{IV}=O intermediates, which have been synthesized using the TMC ligand, are generally unreactive as the steric interaction between the substrate and the cyclam ring blocks the π-attack required for overlap with the FMOs in the S = 1 ground state. However, despite the increased steric bulk trans-axial to the oxo, $[Fe^{IV}{=}O(TBC)(CH_3CN)]^{2+}$ exhibits > 10^2 accelerated rates for both H-atom abstraction and oxo-transfer reactions. From the spectroscopic and computational results presented here, the increased steric interactions of the benzyl groups distort the cyclam ring and weaken the axial and equatorial ligand fields. This stabilizes the $d_{x^2-y^2}$ and d_{z^2} orbitals and decreases the energetic difference between the S = 1 and 2 spin states and thereby allows $[Fe^{IV}{=}O(TBC)(CH_3CN)]^{2+}$ greater accessibility to the S = 2 surface for reactivity.

For the single-electron transfer in a H-atom abstraction reaction, the S = 2 surface yields a linear transition state (~176°) involving a σ-attack of the substrate FMO with the oxygen p_z orbital and limited steric interactions between the substrate and the cyclam ring. This yields a lower steric contribution to the barrier at the transition state for the S = 2 surface. Conversely, reactivity on the S = 1 surface requires π-attack of the substrate FMO with the oxygen $p_{x/y}$ orbital and therefore a side-on approach of the substrate (~144°). In both cyclam complexes, this results in large steric interactions between the substrate and the cyclam ring and produces a large barrier at the transition state (~25 kcal/mol), inconsistent with the observed reaction rates. Thus for an H-atom abstraction reaction by a sterically hindered S = 1 Fe^{IV}=O intermediate, such as the cyclam complexes considered in this study, the rate of reactivity will be determined by the ability to access the S = 2 surface for axial attack.[74]

In contrast to the H-atom abstraction reaction, where the difference in the transition state barrier between the S = 1 and 2 surface reflects the angle of substrate approach, oxo-transfer is a two-electron process requiring both π- and σ-attack of the substrate and good overlap with both the oxo $p_{x/y}$ and p_z orbitals, respectively. On the S = 1 surface, this results in a large elongation of the Fe=O bond and greater cyclam−substrate steric interactions as only the β $d_{xz/yz}$ FMO is energetically available for π-attack. This produces a large transition state barrier. Conversely, on the S = 2 surface the α d_{z^2} orbital is low in energy due to the spin polarization (i.e., electron exchange) and allows the direct σ-attack and the early transfer of a single α electron leading to a high-spin ferric species in the transition state. The addition of this electron into the d_{z^2} orbital weakens both the Fe=O and the trans-axial iron−acetonitrile bonds and allows the Fe=O to move out of the Fe−N equatorial and cyclam hydrogen plane. This results in a smaller angle of the substrate donor orbital and better β π overlap for the transfer of the second electron without a large steric barrier.

6. CONCLUSION

Various factors including the structure and topology of supporting ligands,[16,70,75] the identity of axial ligands,[76,77] the spin states of iron(IV) ion,[37] and the binding of metal ions and proton on the iron−oxo moiety[78−81] have been considered in the reactivities of mononuclear nonheme iron(IV)−oxo complexes. The present study emphasizes the importance of the steric interactions between the substrates and the iron chelate as directed by the FMOs associated with the different spin states in nonheme Fe^{IV}=O reactivity.[49,58,65]

■ ASSOCIATED CONTENT

Supporting Information

Additional tables and figures including EPR, Mössbauer, XAS, and kinetic data as well as supplementary computational results, geometric parameters, and reaction coordinate diagrams. The Cartesian coordinates for all optimized structures, transition states are also included, along with the entire reference 59 and complete crystallographic data (CIF) for the complexes reported in this paper. This material is available free of charge via the Internet at http://pubs.acs.org.

■ AUTHOR INFORMATION

Corresponding Author

wwnam@ewha.ac.kr; edward.solomon@stanford.edu

Notes

The authors declare no competing financial interest.

■ ACKNOWLEDGMENTS

The work was supported by NIH grants GM 40392 (E.I.S.), 5P41RR-001209-32, and 8P41GM 103393-33 (K.O.H.), and by NSF grant MCB 0919027 (E.I.S.). The work at EWU was supported by the NRF/MEST of Korea through CRI, GRL (2010-00353), and WCU (R31-2008-000-10010-0) (W.N.). J.-M.L. acknowledges the support of the Région Rhône-Alpes through contract CIBLE 07 016335. Portions of this research were carried out at the Stanford Synchrotron Radiation Lightsource (SSRL), a Directorate of SLAC National Accelerator Laboratory and an Office of Science User Facility operated for the U.S. Department of Energy (DOE) Office of Science by Stanford University. The SSRL Structural Molecular Biology Program is supported by the DOE Office of Biological and Environmental Research and by the National Institutes of Health, National Institute of General Medical Sciences (including P41GM103393) and the National Center for Research Resources (P41RR001209).

■ REFERENCES

(1) Solomon, E. I.; Brunold, T. C.; Davis, M. I.; Kemsley, J. N.; Lee, S.; Lehnert, N.; Neesse, F.; Skulan, A. J.; Yang, Y.; Zhou, J. *Chem. Rev.* **2000**, *100*, 235−350.

(2) Costas, M.; Mehn, M. P.; Jensen, M. P.; Que, L., Jr. *Chem. Rev.* **2004**, *104*, 939−986.

(3) Krebs, C.; Fujimori, D. G.; Walsh, C. T.; Bollinger, J. M., Jr. *Acc. Chem. Res.* **2007**, *40*, 484−492.

(4) Neidig, M. L.; Decker, A.; Choroba, O. W.; Huang, F.; Kavana, M.; Moran, G. R.; Spencer, J. B.; Solomon, E. I. *Proc. Natl. Acad. Sci. U.S.A.* **2006**, *103*, 12966−12973.

(5) Galonic, D. P.; Barr, E. W.; Walsh, C. T.; Bollinger, J. M., Jr.; Krebs, C. *Nat. Chem. Biol.* **2007**, *3*, 113−116.

(6) Fujimori, D. G.; Barr, E. W.; Matthews, M. L.; Koch, G. M.; Yonce, J. R.; Walsh, C. T.; Bollinger, J. M., Jr.; Krebs, C.; Riggs-Gelasco, P. J. *J. Am. Chem. Soc.* **2007**, *129*, 13408−13409.
(7) Price, J. C.; Barr, E. W.; Tirupati, B.; Bollinger, J. M., Jr.; Krebs, C. *Biochemistry* **2003**, *42*, 7497−7508.
(8) Price, J. C.; Barr, E. W.; Glass, T. E.; Krebs, C.; Bollinger, J. M., Jr. *J. Am. Chem. Soc.* **2003**, *125*, 13008−13009.
(9) Proshlyakov, D. A.; Henshaw, T. F.; Monterosso, G. R.; Ryle, M. J.; Hausinger, R. P. *J. Am. Chem. Soc.* **2004**, *126*, 1022−1023.
(10) Riggs-Gelasco, P. J.; Price, J. C.; Guyer, R. B.; Brehm, J. H.; Barr, E. W.; Bollinger, J. M., Jr.; Krebs, C. *J. Am. Chem. Soc.* **2004**, *2004*, 8108−8109.
(11) Hoffart, L. M.; Barr, E. W.; Guyer, R. B.; Bollinger, J. M., Jr.; Krebs, C. *Proc. Natl. Acad. Sci. U.S.A.* **2006**, *103*, 14738−14743.
(12) Eser, B. E.; Barr, E. W.; Frantom, P. A.; Saleh, L.; Bollinger, J. M., Jr.; Krebs, C.; Fitzpatrick, P. F. *J. Am. Chem. Soc.* **2007**, *129*, 11334−11335.
(13) Panay, A. J.; Lee, M.; Krebs, C.; Bollinger, J. M., Jr.; Fitzpatrick, P. F. *Biochemistry* **2011**, *50*, 1928−1933.
(14) Yoon, J.; Wilson, S. A.; Jang, Y. K.; Seo, M. S.; Nehru, K.; Hedman, B.; Hodgson, K. O.; Solomon, E. I. *Angew. Chem., Int. Ed.* **2009**, *48*, 1257−1260.
(15) Grapperhaus, C. A.; Mienert, B.; Bill, E.; Weyermüller, T.; Wieghardt, K. *Inorg. Chem.* **2000**, *39*, 5306−5317.
(16) Kaizer, J.; Klinker, E. J.; Oh, N. Y.; Rohde, J.-U.; Song, W. J.; Stubna, A.; Kim, J.; Münck, E.; Nam, W.; Que, L., Jr. *J. Am. Chem. Soc.* **2004**, *126*, 472−473.
(17) Lim, M. H.; Rohde, J.-U.; Stubna, A.; Bukowski, M. R.; Costas, M.; Ho, R. Y. N.; Münck, E.; Nam, W.; Que, L., Jr. *Proc. Natl. Acad. Sci. U.S.A.* **2003**, *100*, 3665−3670.
(18) Rohde, J.-U.; In, J.; Lim, M. H.; Brennessel, W. W.; Bukowski, M. R.; Stubna, A.; Münck, E.; Nam, W.; Que, L., Jr. *Science* **2003**, *299*, 1037−1039.
(19) Balland, V.; Charlot, M. F.; Banse, F.; Girerd, J. J.; Mattioli, T. A.; Bill, E.; Bartoli, J. F.; Battioni, P.; Mansuy, D. *Eur. J. Inorg. Chem.* **2004**, 301−308.
(20) Martinho, M.; Banse, F.; Bartoli, J. F.; Mattioli, T. A.; Battioni, P.; Horner, O.; Bourcier, S.; Girerd, J. J. *Inorg. Chem.* **2005**, *44*, 9592−9596.
(21) Klinker, E. J.; Kaizer, J.; Brennessel, W. W.; Woodrum, N. L.; Cramer, C. J.; Que, L., Jr. *Angew. Chem., Int. Ed.* **2005**, *44*, 3690−3694.
(22) Bukowski, M. R.; Koehntop, K. D.; Stubna, A.; Bominaar, E. L.; Halfen, J. A.; Munch, E.; Nam, W.; Que, L., Jr. *Science* **2005**, *310*, 1000−1002.
(23) Jensen, M. P.; Costas, M.; Ho, R. Y. N.; Kaizer, J.; Payeras, A. M. I.; Munck, E.; Que, L. J.; Rohde, J.-U.; Stubna, A. *J. Am. Chem. Soc.* **2005**, *127*, 10512−10525.
(24) Sastri, C. V.; Park, M. J.; Ohta, T.; Jackson, T. A.; Stubna, A.; Seo, M. S.; Lee, J.; Kim, J.; Kitagawa, T.; Münck, E.; Que, L., Jr.; Nam, W. *J. Am. Chem. Soc.* **2005**, *127*, 12494−12495.
(25) Rohde, J.-U.; Que, L., Jr. *Angew. Chem., Int. Ed.* **2005**, *44*, 2255−2258.
(26) Sastri, C. V.; Seo, M. S.; Park, M. J.; Kim, K. M.; Nam, W. *Chem. Commun.* **2005**, 1405−1407.
(27) Bautz, J.; Bukowski, M. R.; Kerscher, M.; Stubna, A.; Comba, P.; Lienke, A.; Münck, E.; Que, L., Jr. *Angew. Chem., Int. Ed.* **2006**, *45*, 5681−5684.
(28) Chanda, A.; Shan, X.; Chakrabarti, M.; Ellis, W. C.; Popescu, D. L.; de Oliveria, F. T.; Wang, D.; Que, L., Jr.; Collins, T. J.; Münck, E.; Bominaar, E. L. *Inorg. Chem.* **2008**, *47*, 3669−3678.
(29) Thibon, A.; England, J.; Martinho, M.; Young, V. G.; Frisch, J. R.; Guillot, R.; Girerd, J. J.; Münck, E.; Que, L., Jr.; Banse, F. *Angew. Chem., Int. Ed.* **2008**, *47*, 7064−7067.
(30) Ray, K.; England, J.; Fiedler, A. T.; Martinho, M.; Münck, E.; Que, L., Jr. *Angew. Chem., Int. Ed.* **2008**, *47*, 8068−8071.
(31) Kim, S. O.; Sastri, C. V.; Seo, M. S.; Kim, J.; Nam, W. *J. Am. Chem. Soc.* **2005**, *127*, 4178−4179.
(32) Bigi, J. P.; Harman, W. H.; Lassalle-Kaiser, B.; Robles, D. M.; Stich, T. A.; Yano, J.; Britt, R. D.; Chang, C. J. *J. Am. Chem. Soc.* **2012**, *134*, 1536−1542.
(33) England, J.; Guo, Y.; Farquhar, E. R.; Young, V. G. J.; Münck, E.; Que, L., Jr. *J. Am. Chem. Soc.* **2010**, *132*, 8635−8644.
(34) England, J.; Martinho, M.; Farquhar, E. R.; Frisch, J. R.; Bominaar, E. L.; Münck, E.; Que, L., Jr. *Angew. Chem., Int. Ed.* **2009**, *48*, 3622−3626.
(35) Lacy, D. C.; Gupta, R.; Stone, K. L.; Greaves, J.; Ziller, J. W.; Hendrich, M. P.; Borovik, A. S. *J. Am. Chem. Soc.* **2010**, *132*, 12188−12190.
(36) Pestovsky, O.; Stoian, S.; Bominaar, E. L.; Que, L., Jr.; Bakac, A. *Angew. Chem., Int. Ed.* **2005**, *117*, 7031−7034.
(37) Janardanan, D.; Wang, Y.; Schyman, P.; Que, L., Jr.; Shaik, S. *Angew. Chem., Int. Ed.* **2010**, *49*, 3342−3345.
(38) Decker, A.; Clay, M. D.; Solomon, E. I. *J. Inorg. Biochem.* **2006**, *100*, 697−706.
(39) Decker, A.; Rohde, J.-U.; Klinker, E. J.; Wong, S. D.; Que, L., Jr.; Solomon, E. I. *J. Am. Chem. Soc.* **2007**, *129*, 15983−15996.
(40) Wong, S. D.; Bell, C. B., III; Liu, L. V.; Kwak, Y.; England, J.; Alp, E. E.; Zhou, J.; Que, L., Jr.; Solomon, E. I. *Angew. Chem., Int. Ed.* **2011**, *50*, 3215−3218.
(41) Armarego, W. L. F.; Chai, C. L. L. E. *Purification of Laboratory Chemicals*, 6th ed.; Pergamon Press: Oxford, U.K., 2009.
(42) Hunter, T. M.; Paisey, S. J.; Park, H.; Cleghorn, L.; Parkin, A.; Parsons, S.; Sadler, P. J. *J. Inorg. Biochem.* **2004**, *98*, 713−719.
(43) Seo, M. S.; Jang, H. G.; Kim, J.; Nam, W. *Bull. Korean Chem. Soc.* **2005**, *26*, 971−974.
(44) Saltzman, H.; Sharefkin, J. G. *Organic Syntheses*; Wiley: New York, 1973; Vol. *V*, p 658.
(45) Evans, D. F. *J. Chem. Soc.* **1959**, 2003−2005.
(46) Evans, D. F.; Jakubovic, D. A. *J. Chem. Soc., Dalton Trans.* **1988**, 2927−2933.
(47) Löliger, J.; Scheffold, R. *J. Chem. Educ.* **1972**, *49*, 646−647.
(48) Sheldrick, G. M. *SHEXTL*, V 6.12; Bruker AXS Inc.: Madison, WI, 2001.
(49) Source: SSRL Biological XAS beam line 9-3, 16-pole, 2-T wiggler, 2.0 mrad beam, SPEAR3 at 3 GeV. Optics: Si(220), liquid nitrogen cooled double crystal monochromator, fully tuned. Premonochromator flat, bent, harmonic rejection vertically collimating Rh-coated Si M0 mirror; and post-30 monochromator bent, cylindrical, Rh-coated Si focusing M1 mirror; 10 keV cutoff, energy resolution 1×10^{-4} $\Delta E/E$.
(50) Cramer, S. P.; Tench, O.; M., Y.; George, G. N. *Nucl. Instrum. Methods. Phys. Rev.* **1988**, *A266*, 586−591 .
(51) Scott, R. A.; Hahn, J. E.; Doniach, S.; Freeman, H. C.; Hodgson, K. O. *J. Am. Chem. Soc.* **1982**, *104*, 5364−5369.
(52) Cramer, S. P.; Hodgson, K. O. *Prog. Inorg. Chem.* **1979**, *25*, 1−39.
(53) DeWitt, J. G.; Bentsen, J. G.; Rosenzweig, A. C.; Hedman, B.; Green, J.; Pilkington, S.; Papaefthymiou, G. C.; Dalton, H.; Hodgson, K. O.; Lippard, S. J. *J. Am. Chem. Soc.* **1991**, *113*, 9219−9235.
(54) Scott, R. A. *Methods Enzymol.* **1985**, *177*, 414−459.
(55) Tenderholt, A.; Hedman, B.; Hodgson, K. O. *AIP Conf. Proc.* **2007**, *882*, 105−107.
(56) Westre, T. E.; Kennepohl, P.; DeWitt, J. G.; Hedman, B.; Hodgson, K. O.; Solomon, E. I. *J. Am. Chem. Soc.* **1997**, *119*, 6297−6314.
(57) George, G. N. *EDG_FIT*; Stanford Synchrotron Radiation Laboratory, Stanford Linear Accelerator Center, Stanford University: Stanford, CA.
(58) George, G. N. *EXAFSPAK*; Stanford Synchrotron Radiation Laboratory, Stanford Linear Accelerator Center, Stanford Synchrotron Radiation Laboratory, Stanford Linear Accelerator Center, Stanford University: Stanford, CA.
(59) Frisch, M. J.et al. *Gaussian 03*, revision C.02; Guassian, Inc.: Wallingford, CT. See SI for full reference.
(60) Becke, A. D. *J. Chem. Phys.* **1993**, *98*, 5648−5652.
(61) Lee, C.; Yang, W.; Parr, R. G. *Phys. Rev. B* **1988**, *37*, 785−789.

(62) Miehlich, B.; Savin, A.; Stroll, H.; Preuss, H. *Chem. Phys. Lett.* **1989**, *157*, 200−206.
(63) Becke, A. D. *Phys. Rev. A: Gen. Phys.* **1988**, *83*, 3098−3100.
(64) Perdew, J. P. *Phys. Rev. B: Condens. Matter* **1986**, *33*, 8822−8824.
(65) Tenderholt, A. L. *QMForge*: A Program to Analyze Quantum Chemistry Calculations, v. 2.1; Stanford University: Stanford CA, 2007; http://qmforge.sourceforge.net.
(66) Laaksonen, L. *J. Mol. Graphics* **1998**, *10*, 33−34.
(67) Bergman, D. L.; Laaksonen, L.; Laaksonen, A. *J. Mol. Graphics Modell.* **1997**, *15*, 301−306.
(68) *The PyMOL Molecular Graphics System*, v. 1.0r2; Schrödinger, LLC: Cambridge, MA , 2006; http://pymol.org.
(69) Fiedler, A. T.; Halfen, H. L.; Halfen, J. A.; Brunold, T. C. *J. Am. Chem. Soc.* **2005**, *127*, 1675−1689.
(70) Seo, M. S.; Kim, N. H.; Cho, K.-B.; So, J. E.; Park, S. K.; Clémancey, M.; Garcia-Serres, R.; Latour, J.-M.; Shaik, S.; Nam, W. *Chem. Sci.* **2011**, *2*, 1039−1045.
(71) Oosterhuis, W. T.; Lang, G. *J. Chem. Phys.* **1973**, *58*, 4757−4765.
(72) Rohde, J.-U.; Torelli, S.; Shan, X.; Lim, M. H.; Klinker, E. J.; Kaizer, J.; Chen, K.; Nam, W.; Que, L., Jr. *J. Am. Chem. Soc.* **2004**, *126*, 16750−16761.
(73) Park, M. J.; Lee, J.; Suh, Y.; Nam, W. *J. Am. Chem. Soc.* **2006**, *128*, 2630−2634.
(74) It is of interest to note that in the case of $[Fe^{IV}{=}O(TMG_3tren)]^{2+}$, which has an $S = 2$ ground state but is not highly reactive as its axial position is sterically hindered, the pentadentate chelate of TMG_3tren may additionally restrict the elongation of the axial ligand and thereby impede the ability of the oxo to move above the ligand plane to lower the steric barrier to reactivity.
(75) Hong, S.; Lee, Y.-M.; Cho, K.-B.; Sundaravel, K.; Cho, J.; Kim, M. J.; Shin, W.; Nam, W. *J. Am. Chem. Soc.* **2011**, *133*, 11876−11879.
(76) Hirao, H.; Que, L., Jr.; Nam, W.; Shaik, S. *Chem.—Eur. J.* **2008**, *14*, 1740−1756.
(77) Sastri, C. V.; Lee, J.; Oh, K.; Lee, Y. J.; Lee, J.; Jackson, T. A.; Ray, K.; Hirao, H.; Shin, W.; Halfen, H. L.; Kim, J.; Que, L., Jr.; Shaik, S.; Nam, W. *Proc. Natl. Acad. Sci. U.S.A.* **2007**, *104*, 19181−19186.
(78) Fukuzumi, S.; Morimoto, Y.; Kotani, Y.; Naumov, P.; Lee, Y.-M.; Nam, W. *Nat. Chem.* **2010**, *2*, 756−759.
(79) Park, J.; Morimoto, Y.; Lee, Y.-M.; Nam, W.; Fukuzumi, S. *J. Am. Chem. Soc.* **2011**, *133*, 5236−5239.
(80) Park, J.; Morimoto, Y.; Lee, Y.-M.; You, Y.; Nam, W.; Fukuzumi, S. *Inorg. Chem.* **2011**, *50*, 11612−11622.
(81) Park, J.; Morimoto, Y.; Lee, Y.-M.; Nam, W.; Fukuzumi, S. *J. Am. Chem. Soc.* **2012**, *134*, 3903−3911.